A fictitious domain method with enhanced interfacial mass conservation for immersed FSI with thin-walled solids

Daniele Corti, Jérôme Diaz, Marina Vidrascu, Dominique Chapelle, Philippe Moireau, Miguel Angel Fernández

▶ **To cite this version:**

Daniele Corti, Jérôme Diaz, Marina Vidrascu, Dominique Chapelle, Philippe Moireau, et al.. A fictitious domain method with enhanced interfacial mass conservation for immersed FSI with thin-walled solids. Journal of Computational Physics, 2026, 556, pp.114754. ⟨10.1016/j.jcp.2026.114754⟩. ⟨hal-04713023v4⟩

HAL Id: hal-04713023

https://hal.science/hal-04713023v4

Submitted on 2 Feb 2026

HAL is a multi-disciplinary open access archive for the deposit and dissemination of scientific research documents, whether they are published or not. The documents may come from teaching and research institutions in France or abroad, or from public or private research centers.

L'archive ouverte pluridisciplinaire **HAL**, est destinée au dépôt et à la diffusion de documents scientifiques de niveau recherche, publiés ou non, émanant des établissements d'enseignement et de recherche français ou étrangers, des laboratoires publics ou privés.

HAL Authorization

A fictitious domain method with enhanced interfacial mass conservation for immersed FSI with thin-walled solids

Daniele C. Corti[a], Jérôme Diaz[b], Marina Vidrascu[a], Dominique Chapelle[b], Philippe Moireau[b] and Miguel A. Fernández[a]

[a]Sorbonne Université & CNRS, UMR 7598 LJLL – Inria, Paris, France
[b]Inria & CMAP, Ecole Polytechnique, CNRS, Institut Polytechnique de Paris, Palaiseau France

ARTICLE INFO

Keywords:
Fluid-structure interaction
Fictitious domain method
3D-shell model
Interfacial mass conservation.

ABSTRACT

In this paper, we extend the low-order fictitious domain method with enhanced mass conservation, introduced in *[ESAIM: Math. Model. Numer. Anal., 58(1):303–333, 2024]*, to fluid-structure interaction with immersed thin-walled solids. The key idea is to improve mass conservation across the interface by imposing a single global velocity constraint on one side of the interface using a scalar Lagrange multiplier. Both 2D and 3D shell models are considered for the description of the solid, including contact between solids. For both models, the interface coupling is enforced on the mid-surface of the shell using a stabilized Lagrange multiplier formulation. Numerical examples in two and three dimensions illustrate the effectiveness of the proposed method, including its successful application to the simulation of aortic heart valve dynamics.

1. Introduction

The numerical simulation of the mechanical interaction between incompressible viscous fluids and immersed moving thin-walled structures plays a fundamental role in a wide variety of engineering fields, ranging from the biomechanics of heart valves to the aeroelasticity of parachutes (see, e.g., [55, 78, 59, 81, 73]). One of the fundamental challenges encountered in the approximation of these systems is the introduction of weak and strong discontinuities in the fluid velocity and pressure fields, respectively, induced by the thin-walled nature of the immersed solid. Preserving these properties at the discrete level is known to play an essential role in the accuracy of the resulting numerical method. In particular, pressure discontinuities across the interface are crucial for ensuring interfacial mass conservation, while discontinuities in the velocity gradient are necessary for achieving optimal accuracy.

Extensive research has been conducted in the development of numerical methods for fluid-structure interaction (FSI), resulting in a wide range of methodologies typically classified as fitted (conforming) or unfitted (non-conforming) mesh methods. In fitted mesh methods, the fluid and structure meshes match at the interface, with the fluid problem typically solved on a deforming mesh that follows the motion of the interface. This facilitates the enforcement of interface conditions, and (weak and strong) discontinuities in the solution can be straightforwardly incorporated at the discrete level, resulting in an optimally accurate method. Noteworthy examples of such methods include those employing the Arbitrary Lagrangian-Eulerian (ALE) formulation in the fluid (see, e.g., [30, 60, 33, 71, 74, 50]) and unified continuum modeling for FSI (see [45, 46, 54]). Nevertheless, the body-fitted nature of the mesh presents challenges whenever the solid undergoes large deflections, particularly in cases of contact between solids, leading to highly distorted fluid meshes that may necessitate remeshing or topological modifications (see, for instance, [1, 75]), thereby increasing computational cost.

Unfitted mesh methods are a widespread approach to avoid these issues. In this class of methods, the fluid mesh is not fitted to the interface, allowing the solid mesh to freely move over the background fluid mesh. Notable methods in this category include the Immersed Boundary (IB) and Immersed Finite Element (IFE) methods (see, e.g., [61, 85, 57, 12, 79]), where the solid acts as an external body force in the fluid equations, and the Fictitious Domain

*Corresponding author: Miguel A. Fernández
daniele.corti@inria.fr (D.C. Corti); jerome.diaz@inria.fr (J. Diaz); marina.vidrascu@inria.fr (M. Vidrascu); dominique.chapelle@inria.fr (D. Chapelle); philippe.moireau@polytechnique.edu (P. Moireau); miguel.fernandez@inria.fr (M.A. Fernández)
ORCID(s): 0000-0002-8388-343X (D.C. Corti); 0000-0003-0794-412X (D. Chapelle); 0000-0001-9996-5213 (P. Moireau); 0000-0003-4694-9118 (M.A. Fernández)

(FD) methods (see, e.g., [70, 4, 28, 31, 3, 15, 47, 11, 16]), where the kinematic constraint is imposed via Lagrange multipliers or penalization. These methods often suffer from spatial inaccuracies arising from the discrete treatment of interface conditions, as well as interfacial mass conservation errors associated with the discrete enforcement of the incompressibility constraint (see, e.g., [62, 47, 72, 16, 21]). Although mesh adaptivity can mitigate these issues, it does not remove them (see, e.g., [42, 8]).

In finite-difference-based IB methods, interfacial mass loss occurs because the interpolated velocity is not divergence-free. A modified scheme that yields a divergence-free interpolated velocity (in an averaged sense) was proposed in [62], but it relies on wide stencils that increase computational complexity. Numerical evidence in [38] indicates that comparable interfacial mass conservation can be achieved using a staggered-grid discretization. This approach was further refined in [5], where a divergence-free velocity interpolation based on an edge-centered discrete vector potential and an adjoint force-spreading formulation were introduced. Recently, mass conservation is enhanced in [41] via regularized delta functions constructed from composite B-splines. This yields divergence-free velocity interpolation while preserving the gradient structure of the spread force (e.g., pressure jumps). Furthermore, in contrast to [5], it also preserves the local computational natural of the original IB method.

In the context of finite volume IB methods, improved mass conservation near the immersed interface has been achieved through various strategies, including the introduction of suitable mass sources and sinks (e.g., [49, 51]), modifications of face fluxes in the continuity equation (e.g., [69, 83]), and the enforcement of pressure jump conditions (e.g., [52]). However, these approaches typically rely on fractional time-stepping schemes for the fluid equations. Cut-cell approaches avoid this issue and achieve strict local mass conservation (see, e.g., [84, 77, 68]), but they are generally complex to implement. More recently, in [35], enhanced mass conservation has been achieved by combining a directional ghost-cell method with a mass-conservative reconstruction of face fluxes.

A simple approach to enhance interfacial mass conservation in finite-element-based FD methods consists in boosting the incompressibility constraint through grad-div penalization in the interfacial zone, although this is known to yield severe ill-conditioning issues (see, e.g., [47, 34, 20, 16]). Alternatively, one can enhance interfacial mass conservation by using discontinuous pressure approximations with higher-order polynomials for velocities (see, e.g., [4, 13, 14, 15]) or by using divergence-free velocity approximations (see [21]). Cut-FEM methods ensure high accuracy by integrating equations solely in the physical region and incorporating stabilizing terms for robustness, but they require intricate computer implementation due to precise tracking of interface intersections and quadrature over arbitrary polygons (see, e.g., [40, 43, 18]). The extended-FEM (XFEM) method, combining cut-FEM with local enrichment, addresses some challenges but introduces additional unknowns (Lagrange multipliers) and potential ill-conditioning (see, e.g., [86, 36, 67]). The Nitsche-XFEM method overcomes these difficulties by combining overlapping meshes with a Nitsche treatment of the interface coupling and suitable stabilization in the interfacial zone for robustness (see [2, 17, 87]). However, the superior accuracy of the Nitsche-XFEM approach comes with increased computational complexity, requiring a more intricate computer implementation and specific tracking of mesh intersections (see, e.g., [2]). It is also worth mentioning the recent cut-FEM method reported in [19], based on the minimal divergence-free element introduced in [26].

In this work, we address the mass conservation issues of finite-element-based FD methods by building on the low-order method introduced in [27] for a Stokes problem with static interface. This approach enhances mass conservation across the interface by imposing a single global velocity constraint on one side of the interface using a scalar Lagrange multiplier. This constraint can alternatively be viewed as an enrichment of the pressure discrete space with a single discontinuous basis function. We formulate and investigate this method in the context of fluid–structure interaction with immersed thin-walled solids, including contact. Two distinct modeling options are considered for the description of the solid: a 2D-shell model under Reissner-Mindlin assumptions (see, e.g., [7, 10, 22]) and a 3D-shell model (see, e.g., [25]). The 3D shell model offers the key advantage of allowing the use of general 3D constitutive relations. We present a unified model coupling framework in which the interface conditions are enforced on the mid-surface of the solid for both the 2D- and the 3D-shell models. Besides its simplicity, in the case of the 3D-shell model, this approach avoids the introduction of fictitious fluid regions resulting from the overlap with the moving solid (see, e.g., [70, 15]). Finally, contact is modeled using a penalty formulation, and a novel semi-implicit mid-point time-stepping scheme inspired by [58] is proposed. The method preserves second-order accuracy and allows for a simple implementation.

The rest of the paper is organized as follows. The continuous setting is outlined in Section 2, where the coupling with the two different shell models is presented within a unified framework. Section 3 describes the proposed fictitious domain approximation with enhanced mass conservation. Section 4 presents a comprehensive numerical

study, including comparisons with alternative approaches, which illustrates the capabilities of the proposed method. Finally, a summary of the main conclusions is provided in Section 5.

2. Problem setting

Let $\Omega \subset \mathbb{R}^3$ be a given fixed domain whose boundary is denoted by $\partial\Omega$. We consider a fluid-structure interaction problem in Ω, involving a thin-walled structure immersed in a viscous, incompressible Newtonian fluid. At time t, the fluid and structure domains are denoted as $\Omega^{\mathrm{f}}(t)$ and $\Omega^{\mathrm{s}}(t)$, respectively. The reference configuration of the structure is denoted by Ω^{s}. The mid-surface of Ω^{s}, denoted by Σ, is assumed to be parametrized by a smooth mapping $\boldsymbol{\phi} : \omega \subset \mathbb{R}^2 \to \mathbb{R}^3$, as $\Sigma = \boldsymbol{\phi}(\omega)$, where ω denotes a reference domain in $\mathbb{R}^2$. We can hence define the couple of tangent vectors

$$\boldsymbol{a}_m(\xi^1, \xi^2) \stackrel{\text{def}}{=} \frac{\partial \boldsymbol{\phi}}{\partial \xi^m}(\xi^1, \xi^2)$$

for $(\xi^1, \xi^2) \in \omega$ and $m = 1, 2$. The unit normal to the mid-surface Σ is given by $\boldsymbol{n}_\Sigma \stackrel{\text{def}}{=} (\boldsymbol{a}_1 \times \boldsymbol{a}_2)\|\boldsymbol{a}_1 \times \boldsymbol{a}_2\|^{-1}$. The reference configuration of the solid is parametrized as the image $\Omega^{\mathrm{s}} = \boldsymbol{\Phi}\big(\omega \times (-1, 1)\big)$ of the mapping $\boldsymbol{\Phi} : \omega \times (-1, 1) \to \mathbb{R}^3$, defined as

$$\boldsymbol{\Phi}(\xi^1, \xi^2, \xi^3) \stackrel{\text{def}}{=} \boldsymbol{\phi}(\xi^1, \xi^2) + \frac{\epsilon \xi^3}{2} \boldsymbol{n}_\Sigma(\xi^1, \xi^2), \tag{1}$$

where $\epsilon > 0$ denotes the thickness of the solid and ξ^3 corresponds to the curvilinear coordinate perpendicular to the mid-surface.

The current position of the structure mid-surface $\Sigma(t)$ is described in terms of the deformation map $\boldsymbol{\psi} : \Sigma \times \mathbb{R}^+ \to \mathbb{R}^3$ as $\Sigma(t) = \boldsymbol{\psi}(\Sigma, t)$. In what follows, we shall use the notation $\boldsymbol{\psi}_t \stackrel{\text{def}}{=} \boldsymbol{\psi}(\cdot, t)$. In this work, the fluid-structure interface will be identified with the solid mid-surface $\Sigma(t)$, by neglecting the shell thickness effects on the interface coupling. Accordingly, the fluid domain is artificially extended up to the solid mid-surface:

$$\Omega^{\mathrm{f}}(t) \stackrel{\text{def}}{=} \Omega \backslash \Sigma(t) \subset \mathbb{R}^3, \tag{2}$$

with boundary $\partial\Omega^{\mathrm{f}}(t) = \Sigma(t) \cup \partial\Omega$. Consequently, the fluid and solid domains artificially overlap within a small region of width ϵ near the interface. This modeling simplification is commonly used when coupling thin-walled solids with 3D media (see, e.g., [23, 47, 50, 16]).

Let us consider the following partition of the boundaries $\partial\Omega = \Gamma^{\mathrm{f}}_{\mathrm{D}} \cup \Gamma^{\mathrm{f}}_{\mathrm{N}}$, $\partial\Omega^{\mathrm{s}} = \Gamma^{\mathrm{s}}_{\mathrm{D}} \cup \Gamma^{\mathrm{s}}_{\mathrm{N}}$ and $\partial\Sigma \cap \Gamma^{\mathrm{s}}_{\mathrm{D}} = \partial\Sigma$, with the subscript D (resp. N) meaning the boundary portion on which Dirichlet (resp. Neumann) condition is enforced. Moreover, assuming that the structure mid-surface $\Sigma(t)$ divides the fluid domain $\Omega^{\mathrm{f}}(t)$ into two subdomains $\Omega^{\mathrm{f}}_1(t)$ and $\Omega^{\mathrm{f}}_2(t)$, with $\Omega^{\mathrm{f}}_1(t) \cap \Omega^{\mathrm{f}}_2(t) = \emptyset$ and $\Sigma(t) = \partial\Omega^{\mathrm{f}}_1(t) \cap \partial\Omega^{\mathrm{f}}_2(t)$, we define $\boldsymbol{n}_1 \stackrel{\text{def}}{=} \boldsymbol{n}_{\Sigma(t)}$ and $\boldsymbol{n}_2 \stackrel{\text{def}}{=} -\boldsymbol{n}_1$ over $\Sigma(t)$ and $\boldsymbol{n}_i \stackrel{\text{def}}{=} \boldsymbol{n}$ on $\partial\Omega^{\mathrm{f}}_i(t) \setminus \Sigma(t)$ for $i = 1, 2$. For a given continuous scalar or tensorial field f defined in $\Omega^{\mathrm{f}}(t)$, possibly discontinuous across $\Sigma(t)$, we define its sided restrictions, noted by f_1 and f_2, as

$$f_1(\boldsymbol{x}) \stackrel{\text{def}}{=} \lim_{\delta \to 0^-} f(\boldsymbol{x} + \delta \boldsymbol{n}_1) \quad f_2(\boldsymbol{x}) \stackrel{\text{def}}{=} \lim_{\delta \to 0^-} f(\boldsymbol{x} + \delta \boldsymbol{n}_2) \qquad \forall \boldsymbol{x} \in \Sigma(t).$$

We also define the following jump operators across the interface $\Sigma(t)$:

$$[\![f]\!] \stackrel{\text{def}}{=} f_1 - f_2, \quad [\![f\boldsymbol{n}]\!] \stackrel{\text{def}}{=} f_1 \boldsymbol{n}_1 + f_2 \boldsymbol{n}_2.$$

2.1. Coupled fluid-structure interaction models

In this section, we introduce two distinct fluid-structure interaction systems that differ in the model used to describe the dynamics of the solid: one where the solid problem is formulated on the mid-surface Σ (see Figure 1a), and another where the solid problem is formulated in the whole domain Ω^{s} (see Figure 1b). Nevertheless, in both cases, the interface coupling is enforced on the solid mid-surface $\Sigma(t)$, and the fluid domain is extended up to this mid-surface via (2).

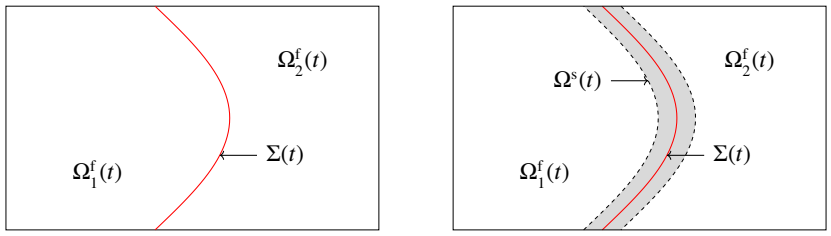

(a) 2D-shell model. (b) 3D-shell model.

Figure 1: Geometric descriptions of a thin-walled solid immersed in a fluid. The fluid subdomains $\Omega_i^f(t)$, $i = 1, 2$, are defined up to the mid-surface $\Sigma(t)$ in both cases.

2.1.1. Coupling with a 2D-shell model

For the first fluid-structure interaction model, we consider the Navier-Stokes equations for homogeneous, incompressible and Newtonian fluids, along with a nonlinear 2D-shell model to describe the behavior of the solid. The coupled problem under consideration is formulated as follows: Find the fluid velocity and pressure $\boldsymbol{u} : \Omega \times \mathbb{R}^+ \to \mathbb{R}^3$, $p : \Omega \times \mathbb{R}^+ \to \mathbb{R}$, the structure displacement and velocity $\boldsymbol{d} : \Sigma \times \mathbb{R}^+ \to \mathbb{R}^3$, $\boldsymbol{u}^s : \Sigma \times \mathbb{R}^+ \to \mathbb{R}^3$ such that

$$\begin{cases} \rho^f \left(\partial_t \boldsymbol{u} + \boldsymbol{u} \cdot \boldsymbol{\nabla} \boldsymbol{u}\right) - \boldsymbol{\nabla} \cdot \boldsymbol{\sigma}^f(\boldsymbol{u}, p) = \boldsymbol{0} & \text{in} \quad \Omega^f(t), \\ \boldsymbol{\nabla} \cdot \boldsymbol{u} = 0 & \text{in} \quad \Omega^f(t), \\ \boldsymbol{u} = \boldsymbol{0} & \text{on} \quad \Gamma_D^f, \\ \boldsymbol{\sigma}^f(\boldsymbol{u}, p)\boldsymbol{n} = \boldsymbol{0} & \text{on} \quad \Gamma_N^f, \end{cases} \tag{3}$$

$$\begin{cases} \rho^s \epsilon \partial_t \boldsymbol{u}^s + \boldsymbol{L}(\boldsymbol{d}) = \boldsymbol{T} & \text{on} \quad \Sigma, \\ \boldsymbol{u}^s = \partial_t \boldsymbol{d} & \text{on} \quad \Sigma, \\ \boldsymbol{d} = \boldsymbol{0} & \text{on} \quad \partial\Sigma. \end{cases} \tag{4}$$

$$\begin{cases} \boldsymbol{\psi} = \boldsymbol{I}_\Sigma + \boldsymbol{d} & \text{on} \quad \Sigma, \quad \Sigma(t) = \boldsymbol{\psi}_t(\Sigma), \quad \Omega^f(t) = \Omega \backslash \Sigma(t), \\ \boldsymbol{u} = \boldsymbol{u}^s \circ \boldsymbol{\psi}_t^{-1} & \text{on} \quad \Sigma(t), \\ \displaystyle\int_\Sigma \boldsymbol{T} \cdot \boldsymbol{w} = -\int_{\Sigma(t)} [\![\boldsymbol{\sigma}^f(\boldsymbol{u}, p)\boldsymbol{n}]\!] \cdot \boldsymbol{w} \circ \boldsymbol{\psi}_t^{-1} & \forall\, \boldsymbol{w} \in \boldsymbol{W}. \end{cases} \tag{5}$$

The symbols ρ^f and ρ^s represent the fluid and solid mass densities, respectively. The fluid Cauchy stress tensor is given by

$$\boldsymbol{\sigma}^f(\boldsymbol{u}, p) \stackrel{\text{def}}{=} 2\mu\boldsymbol{\varepsilon}(\boldsymbol{u}) - p\boldsymbol{I},$$

where μ denotes the fluid dynamic viscosity, and the strain rate tensor $\boldsymbol{\varepsilon}(\boldsymbol{u})$ is defined as

$$\boldsymbol{\varepsilon}(\boldsymbol{u}) \stackrel{\text{def}}{=} \frac{1}{2}\left(\boldsymbol{\nabla}\boldsymbol{u} + \boldsymbol{\nabla}\boldsymbol{u}^T\right).$$

Here, the nonlinear surface operator $\boldsymbol{L}$ describes the elastic behavior of the structure. The relations in (5) respectively enforce the geometrical compatibility, the kinematic and the dynamic coupling at the interface between the fluid and the solid media. Here, the symbol $\boldsymbol{W}$ stands for the space of admissible solid displacements, and $\boldsymbol{T}$ represents the fluid traction acting on the reference configuration of the interface.

2.1.2. Coupling with a 3D-shell model

In the second fluid-structure interaction model, we consider the following 3D-shell model for the solid:

$$\rho^s \int_{\Omega^s} \partial_t \boldsymbol{u}^s \cdot \boldsymbol{w} + \int_{\Omega^s} \boldsymbol{\sigma}^s(\boldsymbol{d}) : D_{\boldsymbol{d}}\boldsymbol{E} \cdot \boldsymbol{w} = \int_\Sigma \boldsymbol{T} \cdot \boldsymbol{w} \tag{6}$$

for all $\boldsymbol{w} \in \boldsymbol{W}$ and where the 3D-shell reduced space $\boldsymbol{W}$ is given by (see, e.g., [25])

$$\boldsymbol{W} \stackrel{\text{def}}{=} \left\{ \boldsymbol{w} \in [H^1_{\Gamma_{\mathrm{D}}}(\Omega^{\mathrm{s}})]^3 \,:\, \boldsymbol{w} = \boldsymbol{w}_0 + \boldsymbol{w}_1 \xi^3 + \boldsymbol{w}_2 (\xi^3)^2, \quad \boldsymbol{w}_i \in \left[H^1(\Sigma)\right]^3, \quad i = 0, 1, 2 \right\}. \tag{7}$$

Here, ξ^3 corresponds to the transverse coordinate defined by (1). Note that the vector fields $\boldsymbol{w}_i$, for $i = 0, 1, 2$, are defined only on the mid-surface Σ and, hence, they are only functions of the tangential coordinates (ξ^1, ξ^2). Furthermore, in contrast to (4), no plane stress assumption is made in (7), which facilitates the use of non-linear constitutive laws for the solid (second Piola–Kirchhoff) stress tensor $\boldsymbol{\sigma}^{\mathrm{s}}(\boldsymbol{d})$. For instance, for a hyperelastic material we have $\boldsymbol{\sigma}^{\mathrm{s}} = \frac{\partial W_{\mathrm{e}}}{\partial \boldsymbol{E}}$, where W_{e} stands for the hyperelastic potential and $\boldsymbol{E}$ denotes the Green-Lagrange strain tensor.

In this framework, the resulting coupled fluid-structure problem is formulated as follows: Find the fluid velocity and pressure $\boldsymbol{u} : \Omega \times \mathbb{R}^+ \to \mathbb{R}^3$, $p : \Omega \times \mathbb{R}^+ \to \mathbb{R}$, the solid displacement and velocity $\boldsymbol{d}(t), \boldsymbol{u}^{\mathrm{s}}(t) \in \boldsymbol{W}$, for $t \in \mathbb{R}^+$, such that the relations (3), (6) and (5) are satisfied.

Remark 1. It is worth emphasizing that, in the coupled problems considered above (viz., (3)–(5) and (3), (6), (5)), the fluid-structure interface is identified with the solid mid-surface $\Sigma(t)$, thereby neglecting shell thickness effects in the interface coupling. In the case of the 3D-shell model, this assumption neglects in particular the fact that the velocity on the physical boundary may differ from that on the mid-surface. Note also that the parameter ρ^{s} in (4) and (6) denotes the true solid mass density, rather than an excess mass density (see, e.g., [12]). Since the thickness ϵ of the thin-walled solid is assumed to be small, the resulting mass and momentum double-counting effets in the overlap region (of width ϵ) are expected to be negligible (see, e.g., [23]). Finally, since the solid is geometrically represented by its mid-surface in the coupling with the fluid, it does not displace fluid. Consequently, no buoyancy force acts on the solid in the presence of gravity. This limitation can be circumvent by introducing a buoyancy force as a source term in the solid equations using a static approximation (see, e.g., [50]).

2.1.3. Contact model

In this work, contact between immersed thin-walled solids will be modeled by adding a non-penetration condition to (4) and (6). More precisely, we propose to enforce the contact constraint on the solid mid-surface $\Sigma(t)$, for both the 2D- and the 3D-shell models:

$$\operatorname{dist}\big(\boldsymbol{x}, \Sigma(t)\big) \geq 0 \quad \forall \boldsymbol{x} \in \Sigma(t), \tag{8}$$

where $\operatorname{dist}\big(\boldsymbol{x}, \Sigma(t)\big)$ stands for the signed distance between $\boldsymbol{x}$ and its potential contact region in $\Sigma(t)$.

2.2. Variational formulation

The two coupled problems introduced above (i.e., (3)–(5) and (3), (6), (5)) can be cast into a single variational formulation which treats the kinematic and dynamic coupling in a weak fashion by using Lagrange multipliers. To this purpose, we introduce the following functional spaces for the velocity, pressure and Lagrange multiplier:

$$\boldsymbol{V} \stackrel{\text{def}}{=} [H^1_{\Gamma^{\mathrm{f}}_{\mathrm{D}}}(\Omega)]^3, \qquad Q \stackrel{\text{def}}{=} L^2(\Omega), \qquad \boldsymbol{\Lambda}(t) \stackrel{\text{def}}{=} [L^2(\Sigma(t))]^3.$$

We also introduce the standard fluid tri-linear form $a^{\mathrm{f}} : \boldsymbol{V} \times \big(\boldsymbol{V} \times Q\big) \times \big(\boldsymbol{V} \times Q\big) \to \mathbb{R}$ given by

$$a^{\mathrm{f}}\big(\boldsymbol{z}; (\boldsymbol{u}, p), (\boldsymbol{v}, q)\big) \stackrel{\text{def}}{=} \rho^{\mathrm{f}} \int_\Omega \boldsymbol{z} \cdot \nabla \boldsymbol{u} \cdot \boldsymbol{v} + 2\mu \int_\Omega \boldsymbol{\varepsilon}(\boldsymbol{u}) : \boldsymbol{\varepsilon}(\boldsymbol{v}) - \int_\Omega p \boldsymbol{\nabla} \cdot \boldsymbol{v} + \int_\Omega q \boldsymbol{\nabla} \cdot \boldsymbol{u}, \tag{9}$$

In what follows, the abstract form $a^{\mathrm{s}} : \boldsymbol{W} \times \boldsymbol{W} \to \mathbb{R}$ represents the weak formulation of the solid elastic contributions. In particular, $a^{\mathrm{s}}(\boldsymbol{d}; \boldsymbol{w})$ is assumed to be linear only with respect to the second argument. For the solid inertial contributions, the L^2-inner product $\big(\cdot, \cdot\big)_{\mathrm{s}}$ is defined according to the considered model, namely:

$$\big(\boldsymbol{d}, \boldsymbol{w}\big)_{\mathrm{s}} \stackrel{\text{def}}{=} \begin{cases} \epsilon \displaystyle\int_\Sigma \boldsymbol{d} \cdot \boldsymbol{w} & \text{for the 2D-shell model (4),} \\ \displaystyle\int_{\Omega^{\mathrm{s}}} \boldsymbol{d} \cdot \boldsymbol{w} & \text{for the 3D-shell model (6).} \end{cases}$$

The resulting weak formulation of the fluid-structure interaction problems considered in Sections 2.1.1–2.1.2 reads as follows: For $t > 0$, find $\big(\boldsymbol{u}(t), p(t), \boldsymbol{\lambda}(t), \boldsymbol{d}(t)\big) \in \boldsymbol{V} \times Q \times \boldsymbol{\Lambda}(t) \times \boldsymbol{W}$, with $\boldsymbol{u}^{\mathrm{s}} = \partial_t \boldsymbol{d}$, such that

$$\rho^{\mathrm{f}} \int_{\Omega} \partial_t \boldsymbol{u} \cdot \boldsymbol{v} + a^{\mathrm{f}}\big(\boldsymbol{u}; (\boldsymbol{u}, p), (\boldsymbol{v}, q)\big) + \rho^{\mathrm{s}}\big(\partial_t \boldsymbol{u}^{\mathrm{s}}, \boldsymbol{w}\big)_{\mathrm{s}} + a^{\mathrm{s}}\big(\boldsymbol{d}; \boldsymbol{w}\big) - \int_{\Sigma(t)} \boldsymbol{\lambda} \cdot \big(\boldsymbol{v} - \boldsymbol{w} \circ \boldsymbol{\psi}_t^{-1}\big) + \int_{\Sigma(t)} \boldsymbol{\xi} \cdot \big(\boldsymbol{u} - \boldsymbol{u}^{\mathrm{s}} \circ \boldsymbol{\psi}_t^{-1}\big) = 0 \quad (10)$$

for all $(\boldsymbol{v}, q, \boldsymbol{\xi}, \boldsymbol{w}) \in \boldsymbol{V} \times Q \times \boldsymbol{\Lambda}(t) \times \boldsymbol{W}$. Using a standard argument of integration by parts in $\Omega^{\mathrm{f}}(t)$, it can be shown that problem (10) is equivalent to the above strong formulations with $\boldsymbol{\lambda} = [\![\boldsymbol{\sigma}^{\mathrm{f}}(\boldsymbol{u}, p)\boldsymbol{n}]\!]$ on $\Sigma(t)$.

By taking alternatively $\boldsymbol{w} = \boldsymbol{0}$ and $(\boldsymbol{v}, q) = (\boldsymbol{0}, 0)$ in (10), we get the following coupled partitioned weak formulations:

- Fluid subproblem: For $t > 0$, find $\big(\boldsymbol{u}(t), p(t), \boldsymbol{\lambda}(t)\big) \in \boldsymbol{V} \times Q \times \boldsymbol{\Lambda}(t)$ such that

$$\rho^{\mathrm{f}} \int_{\Omega} \partial_t \boldsymbol{u} \cdot \boldsymbol{v} + a^{\mathrm{f}}\big(\boldsymbol{u}; (\boldsymbol{u}, p), (\boldsymbol{v}, q)\big) - \int_{\Sigma(t)} \boldsymbol{\lambda} \cdot \boldsymbol{v} + \int_{\Sigma(t)} \boldsymbol{\xi} \cdot \big(\boldsymbol{u} - \boldsymbol{u}^{\mathrm{s}} \circ \boldsymbol{\psi}_t^{-1}\big) = 0 \quad (11)$$

  for all $(\boldsymbol{v}, q, \boldsymbol{\xi}) \in \boldsymbol{V} \times Q \times \boldsymbol{\Lambda}(t)$;

- Solid subproblem: For $t > 0$, find $\boldsymbol{d}(t) \in \boldsymbol{W}$, with $\boldsymbol{u}^{\mathrm{s}} = \partial_t \boldsymbol{d}$, such that

$$\rho^{\mathrm{s}}\big(\partial_t \boldsymbol{u}^{\mathrm{s}}, \boldsymbol{w}\big)_{\mathrm{s}} + a^{\mathrm{s}}\big(\boldsymbol{d}; \boldsymbol{w}\big) = -\int_{\Sigma(t)} \boldsymbol{\lambda} \cdot \boldsymbol{w} \circ \boldsymbol{\psi}_t^{-1} \quad (12)$$

  for all $\boldsymbol{w} \in \boldsymbol{W}$.

2.2.1. Penalized contact constraint

In the case of contacting solids, the constraint (8) will be approximated using a penalty method, with the corresponding energy term

$$\mathcal{W}_{\mathrm{c}}\big(\boldsymbol{d}(t)\big) \overset{\mathrm{def}}{=} \int_{\Sigma(t)} \frac{\kappa_{\mathrm{c}}}{2} \Big|\mathrm{dist}\big(\boldsymbol{x}, \Sigma(t)\big)\Big|_{-}^{2}, \quad (13)$$

where $\kappa_{\mathrm{c}} > 0$ denotes the penalty parameter and $|x|_{-} \overset{\mathrm{def}}{=} \min\{0, x\}$. Note that this requires the evaluation of the gradient of the distance function with respect to the displacement field $\boldsymbol{d}$. The difficulty is that we must calculate the distance to a surface that moves according to the deformation. Let $\boldsymbol{\pi}_{\Sigma(t)}$ be the closest point projection operator on the potential contact zones of $\Sigma(t)$ (see, e.g., [58, 63]), we have

$$\begin{aligned}
\boldsymbol{\nabla}_{\boldsymbol{d}} \mathrm{dist}\big(\boldsymbol{x}, \Sigma(t)\big)\boldsymbol{w} &= -\boldsymbol{\nabla}_{\boldsymbol{d}} \big((\boldsymbol{\pi}_{\Sigma(t)}(\boldsymbol{x}) - \boldsymbol{x}) \cdot \boldsymbol{n}_{\Sigma(t)}(\boldsymbol{\pi}_{\Sigma(t)}(\boldsymbol{x}))\big)\boldsymbol{w} \\
&= \big(\boldsymbol{\nabla}_{\boldsymbol{d}} \boldsymbol{x}\boldsymbol{w}\big) \cdot \boldsymbol{n}_{\Sigma(t)}(\boldsymbol{\pi}_{\Sigma(t)}(\boldsymbol{x})) - \big(\boldsymbol{\nabla}_{\boldsymbol{d}} \boldsymbol{\pi}_{\Sigma(t)}(\boldsymbol{x})\boldsymbol{w}\big) \cdot \boldsymbol{n}_{\Sigma(t)}(\boldsymbol{\pi}_{\Sigma(t)}(\boldsymbol{x})) \\
&\quad - \big(\boldsymbol{\nabla}_{\boldsymbol{d}} \boldsymbol{n}_{\Sigma(t)}(\boldsymbol{\pi}_{\Sigma(t)}(\boldsymbol{x}))\boldsymbol{w}\big) \cdot \big(\boldsymbol{\pi}_{\Sigma(t)}(\boldsymbol{x}) - \boldsymbol{x}\big) \\
&= \boldsymbol{n}_{\Sigma(t)}(\boldsymbol{\pi}_{\Sigma(t)}(\boldsymbol{x})) \cdot \big(\boldsymbol{w}(\boldsymbol{x}) - \boldsymbol{w}(\boldsymbol{\pi}_{\Sigma(t)}(\boldsymbol{x}))\big).
\end{aligned}$$

Therefore, the variational term associated to (13) is given by

$$a_{\mathrm{c}}^{\mathrm{s}}(\boldsymbol{d}; \boldsymbol{w}) \overset{\mathrm{def}}{=} \int_{\Sigma(t)} \kappa_{\mathrm{c}} \Big|\mathrm{dist}\big(\boldsymbol{x}, \Sigma(t)\big)\Big|_{-} \boldsymbol{n}_{\Sigma(t)}(\boldsymbol{\pi}_{\Sigma(t)}(\boldsymbol{x})) \cdot \big(\boldsymbol{w}(\boldsymbol{x}) - \boldsymbol{w}(\boldsymbol{\pi}_{\Sigma(t)}(\boldsymbol{x}))\big), \quad (14)$$

which must be added to the solid elastic contribution $a^{\mathrm{s}}(\boldsymbol{d}; \boldsymbol{w})$ in (10) and (12).

3. Numerical approximation

In order to ease the presentation, we assume that Ω, Ω^{s} and Σ are polyhedral or polygonal domains. We consider a family of triangulations $\{\mathcal{T}_h^{\Omega}\}_{0<h<1}$ of Ω made of tetrahedra. Note that each mesh $\mathcal{T}_h^{\Omega}$ is not necessarily fitted to Σ. For the 3D-shell case, we first consider a family of quadrilateral meshes of the mid-surface Σ, denoted by $\{\mathcal{T}_{\mathcal{H}}^{\mathrm{q}}\}_{0<\mathcal{H}<1}$. A volumic mesh $\mathcal{T}_{\mathcal{H}}^{\Omega^{\mathrm{s}}}$ of Ω^{s}, made of $\mathbb{Q}_1 - \mathbb{P}_2$ prismatic elements, is then obtained by extrusion of $\mathcal{T}_{\mathcal{H}}^{\mathrm{q}}$ along the normal

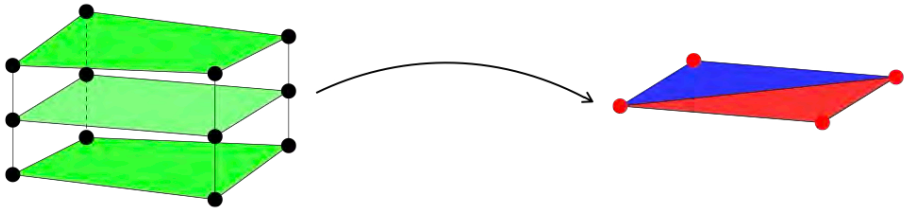

Figure 2: Example of $\mathbb{Q}_1 - \mathbb{P}_2$ prismatic element of $\mathcal{T}_{\mathcal{H}}^{\Omega^s}$ (left) and its corresponding triangulated mid-surface element of $\mathcal{T}_{\mathcal{H}}^{\Sigma}$ (right).

direction $\boldsymbol{n}_\Sigma$ at each node of $\mathcal{T}_{\mathcal{H}}^{\mathrm{q}}$ (see Figure 2(left)). A triangular mesh $\mathcal{T}_{\mathcal{H}}^{\Sigma}$ of Σ is then obtained by dividing each element of $\mathcal{T}_{\mathcal{H}}^{\mathrm{q}}$ into two triangles, so that $\mathcal{T}_{\mathcal{H}}^{\Sigma}$ and $\mathcal{T}_{\mathcal{H}}^{\mathrm{q}}$ share the same nodes. For the 2D-shell case, the mid-surface mesh $\mathcal{T}_{\mathcal{H}}^{\Sigma}$ is also made of triangular elements. The triangular mid-surface mesh $\mathcal{T}_{\mathcal{H}}^{\Sigma}$ serves as geometrical support for the discrete enforcement of both the coupling and contact conditions.

In what follows, the symbol $\tau > 0$ represents the time-step length, $t_n \overset{\text{def}}{=} n\tau$, $n \in \mathbb{N}$, and

$$\partial_\tau x^n \overset{\text{def}}{=} \frac{x^n - x^{n-1}}{\tau}, \quad x^{n-1/2} \overset{\text{def}}{=} \frac{x^n + x^{n-1}}{2},$$

respectively denote the first-order backward difference and the mid-point value.

3.1. Discrete solid problem

The solid subproblem (12) is discretized in time using the mid-point scheme. As regards the spatial discretization, different discrete spaces $\boldsymbol{W}_{\mathcal{H}}$ are considered for the approximation of the solid space $\boldsymbol{W}$, depending on whether a 2D- or a 3D-shell model is used. Specifically, for the 2D-shell model the space $\boldsymbol{W}_{\mathcal{H}} \subset \boldsymbol{W}$ is defined as the space of continuous piecewise affine finite elements over the triangulation $\mathcal{T}_{\mathcal{H}}^{\Sigma}$. In contrast, for the 3D-shell model the space $\boldsymbol{W}_{\mathcal{H}} \subset \boldsymbol{W}$ is made of continuous piecewise $\mathbb{Q}_1 \otimes \mathbb{P}_2$ polynomials. The choice of $\mathbb{P}_2$ polynomials along the orthogonal direction to the mid-surface ensures asymptotic compatibility with the full 3D model, while the $\mathbb{Q}_1$ approximation along the tangential coordinates brings computational efficiency. Additionally, in both cases, an MITC (Mixed Interpolation of Tensorial Components) re-interpolation procedure of Green-Lagrange strain components is used to mitigate numerical locking phenomena, especially for small thickness values (see, e.g., [53, 24]). Hereafter, the form $a^{\mathrm{s}}_{\mathcal{H}} : \boldsymbol{W}_{\mathcal{H}} \times \boldsymbol{W}_{\mathcal{H}} \to \mathbb{R}$ denotes the resulting approximation of the solid elastic variational term $a^{\mathrm{s}}(\boldsymbol{d}; \boldsymbol{w})$.

The proposed fully discrete solid subproblem reads as follows: Find $\boldsymbol{d}^n_{\mathcal{H}} \in \boldsymbol{W}_{\mathcal{H}}$, with $\boldsymbol{u}^{\mathrm{s},n-1/2}_{\mathcal{H}} = \partial_\tau \boldsymbol{d}^n_{\mathcal{H}}$, such that

$$\rho^{\mathrm{s}}\big(\partial_\tau \boldsymbol{u}^{\mathrm{s},n-1/2}_{\mathcal{H}}, \boldsymbol{w}_{\mathcal{H}}\big)_{\mathrm{s}} + a^{\mathrm{s}}_{\mathcal{H}}\big(\boldsymbol{d}^{n-1/2}_{\mathcal{H}}; \boldsymbol{w}_{\mathcal{H}}\big) = -\int_{\Sigma^{n-1}} \boldsymbol{\lambda}^n_{\mathcal{H}} \cdot \boldsymbol{w}_{\mathcal{H}} \circ \big(\boldsymbol{\psi}^{n-1}_{\mathcal{H}}\big)^{-1} \tag{15}$$

for all $\boldsymbol{w}_{\mathcal{H}} \in \boldsymbol{W}_{\mathcal{H}}$. The interface location can then be updated as follows:

$$\boldsymbol{\psi}^n_{\mathcal{H}} = \boldsymbol{I}_\Sigma + \boldsymbol{d}^n_{\mathcal{H}} \quad \text{on} \quad \Sigma, \qquad \Sigma^n = \boldsymbol{\psi}^n_{\mathcal{H}}(\Sigma). \tag{16}$$

Here, the current configuration of the solid mid-surface Σ^n results from the deformation of the triangular mid-surface mesh $\mathcal{T}_{\mathcal{H}}^{\Sigma}$ through the deformation map $\boldsymbol{\psi}^n_{\mathcal{H}}$. In the case of coupling with the 3D-shell model, since this map is piecewise $\mathbb{Q}1$ on the mid-surface, it is interpolated on the triangular mesh $\mathcal{T}_{\mathcal{H}}^{\Sigma}$ prior to deformation. This interpolation step is omitted in (16) for clarity of presentation.

Note that the dynamic coupling in (15) is enforced on the previous configuration of the solid mid-surface Σ^{n-1}. Furthermore, the discrete Lagrange multiplier $\boldsymbol{\lambda}^n_{\mathcal{H}}$ is not known; its evaluation will be described in Section 3.2, together with the approximation of the fluid subproblem (11).

3.1.1. Penalized contact time-stepping approximation

Following the ideas introduced in [58] for stabilization operators based on distance computation, we propose to discretize in time the contact term $a^{\mathrm{s}}_{\mathrm{c}}(\boldsymbol{d}; \boldsymbol{w})$ in a semi-implicit fashion. As a mid-point based time discretization has

been considered for the solid, an energy balanced discretization would be given by a mid-point approximation of $a_{\rm c}^{\rm s}$, namely

$$a_{\rm c}^{\rm s}(\boldsymbol{d}^{n-\frac{1}{2}};\boldsymbol{w}) = \int_{\Sigma^{n-\frac{1}{2}}} \kappa_{\rm c}\Big|{\rm dist}(\boldsymbol{x},\Sigma^{n-1/2})\Big|_{-}\boldsymbol{n}_{\Sigma^{n-1/2}}(\boldsymbol{\pi}_{\Sigma^{n-1/2}}(\boldsymbol{x}))\cdot\big(\boldsymbol{w}(\boldsymbol{x})-\boldsymbol{w}(\boldsymbol{\pi}_{\Sigma^{n-1/2}}(\boldsymbol{x}))\big), \tag{17}$$

where, for simplicity of presentation, the spatial discretization subscript $_{\mathcal{H}}$ has been omitted. However, this discretization requires the differentiation of (17) with respect to the displacement. This leads to the computation of the derivative of $\boldsymbol{n}_{\Sigma^{n-1/2}}(\boldsymbol{\pi}_{\Sigma^{n-1/2}}(\boldsymbol{x}))$, hence introducing the curvature of $\Sigma^{n-1/2}$. In order to overcome this difficulty, we introduce a semi-implicit version of (17) based on a linearization argument. To this purpose, we introduce the following discretization

$$\begin{aligned}
a_{\rm c}^{n-1/2\sharp}(\boldsymbol{d}^{n-\frac{1}{2}};\boldsymbol{w}) &\overset{\rm def}{=} \int_{\Sigma^{n-1/2\sharp}} \kappa_{\rm c}\Big|{\rm dist}(\boldsymbol{x},\Sigma^{n-1/2\sharp})\Big|_{-}\boldsymbol{n}_{\Sigma^{n-1/2\sharp}}(\boldsymbol{\pi}_{\Sigma^{n-1/2\sharp}}(\boldsymbol{x}))\cdot(\boldsymbol{w}(\boldsymbol{x})-\boldsymbol{w}(\boldsymbol{\pi}_{\Sigma^{n-1/2\sharp}}(\boldsymbol{x})))\\
&+\int_{\Sigma^{n-1/2\sharp}} \kappa_{\rm c} H\big(-{\rm dist}(\boldsymbol{x},\Sigma^{n-1/2\sharp})\big)\boldsymbol{n}_{\Sigma^{n-1/2\sharp}}(\boldsymbol{\pi}_{\Sigma^{n-1/2\sharp}}(\boldsymbol{x}))\cdot\Big(\boldsymbol{w}(\boldsymbol{x})-\boldsymbol{w}(\boldsymbol{\pi}_{\Sigma^{n-1/2\sharp}}(\boldsymbol{x}))\Big)\\
&\quad\times\boldsymbol{n}_{\Sigma^{n-1/2\sharp}}(\boldsymbol{\pi}_{\Sigma^{n-1/2\sharp}}(\boldsymbol{x}))\cdot\Big[\Big(\boldsymbol{d}^{n-1/2}(\boldsymbol{x})-\boldsymbol{d}^{n-1/2\sharp}(\boldsymbol{x})\Big)-\Big(\boldsymbol{d}^{n-1/2}(\boldsymbol{\pi}_{\Sigma^{n-1/2\sharp}}(\boldsymbol{x}))-\boldsymbol{d}^{n-1/2\sharp}(\boldsymbol{\pi}_{\Sigma^{n-1/2\sharp}}(\boldsymbol{x}))\Big)\Big],
\end{aligned} \tag{18}$$

with H the Heaviside function and $\Sigma^{n-1/2\sharp}$ the surface associated to the extrapolated displacement $\boldsymbol{d}^{n-1/2\sharp}$, for instance,

$$\boldsymbol{d}^{n-1/2\sharp} \overset{\rm def}{=} \boldsymbol{d}^{n-1}+\frac{\tau}{2}\boldsymbol{u}^{{\rm s},n-1} = \frac{3}{2}\boldsymbol{d}^{n-1}-\frac{1}{2}\boldsymbol{d}^{n-2}.$$

The consistency of this time discretization is justified by the following computation. As already obtained in [58] in a similar context, we have

$$\begin{aligned}
&a_{\rm c}\big(\boldsymbol{d}^{n-1/2};\boldsymbol{w}\big)-a_{\rm c}^{n-1/2\sharp}\big(\boldsymbol{d}^{n-1/2};\boldsymbol{w}\big) = -\frac{\kappa_{\rm c}}{2}\int_{\Sigma^{n-1/2\sharp}}\Big|{\rm dist}(\boldsymbol{x},\Sigma^{n-1/2\sharp})\Big|_{-}{\rm D}\boldsymbol{n}_{\Sigma^{n-1/2\sharp}}(\boldsymbol{\pi}_{\Sigma^{n-1/2\sharp}}(\boldsymbol{x}))\\
&\cdot\Big[\Big(\boldsymbol{d}^{n-1/2}(\boldsymbol{x})-\boldsymbol{d}^{n-1/2\sharp}(\boldsymbol{x})\Big)-\Big(\boldsymbol{d}^{n-1/2}(\boldsymbol{\pi}_{\Sigma^{n-1/2\sharp}}(\boldsymbol{x}))-\boldsymbol{d}^{n-1/2\sharp}(\boldsymbol{\pi}_{\Sigma^{n-1/2\sharp}}(\boldsymbol{x}))\Big)\Big]+O\left(\frac{\kappa_{\rm c}}{2}\left\|\boldsymbol{d}^{n-1/2}-\boldsymbol{d}^{n-1/2\sharp}\right\|^2\right).
\end{aligned}$$

We have seen that $\kappa_{\rm c}\Big|{\rm dist}(\boldsymbol{x},\Sigma^{n-1/2\sharp})\Big|_{-}$ is the contact force per surface unit, hence it remains finite. This leads to the relation

$$a_{\rm c}(\boldsymbol{d}^{n-1/2};\boldsymbol{w})-a_{\rm c}^{n-1/2\sharp}(\boldsymbol{d}^{n-1/2};\boldsymbol{w}) = O\Big(\frac{\kappa_{\rm c}}{2}\left\|\boldsymbol{d}^{n-1/2}-\boldsymbol{d}^{n-1/2\sharp}\right\|\Big)O\Big(1+\kappa_{\rm c}\left\|\boldsymbol{d}^{n-1/2}-\boldsymbol{d}^{n-1/2\sharp}\right\|^2\Big).$$

Therefore, with the above choice of extrapolation, we finally get

$$a_{\rm c}(\boldsymbol{d}^{n-1/2};\boldsymbol{w})-a_{\rm c}^{n-1/2\sharp}(\boldsymbol{d}^{n-1/2};\boldsymbol{w}) = O\big(\tau^2+\kappa_{\rm c}\tau^4\big).$$

As a consequence, for any large value of $\kappa_{\rm c}$ there exists a sufficiently small time-step length τ such that the proposed semi-implicit time scheme (based on a linearization procedure (18)) does not alter the second-order accuracy of the mid-point scheme.

3.2. Discrete fluid problem

The fluid subproblem (11) is discretized in time using a semi-implicit backward-Euler scheme in which the geometrical non-linearities are treated in an explicit fashion. More precisely, at time level n, the kinematic coupling condition is enforced on the discrete interface configuration Σ^{n-1} at the previous time-step. The spatial approximation of (11) is based on the enhanced mass conservation approach proposed and analyzed in [27], which is here extended to the case of a moving interface. To this purpose, we first consider the following standard spaces of continuous piecewise affine functions:

$$X_h^{\rm f} \overset{\rm def}{=} \big\{v_h\in C^0(\Omega): v_h|_K\in\mathbb{P}_1(K),\quad\forall K\in\mathcal{T}_h^{\Omega}\big\},\quad X_{\mathcal{H}}^{\Sigma}\overset{\rm def}{=}\big\{\chi_{\mathcal{H}}\in C^0(\Sigma):\chi_{\mathcal{H}}|_K\in\mathbb{P}_1(T),\quad\forall T\in\mathcal{T}_{\mathcal{H}}^{\Sigma}\big\}.$$

We consider the following low-order finite element spaces for the approximation of the fluid velocity and of the Lagrange multiplier:

$$\boldsymbol{V}_h \overset{\text{def}}{=} [X_h^{\mathrm{f}}]^3 \cap \boldsymbol{V}, \quad \boldsymbol{\Lambda}_{\mathcal{H}}^n \overset{\text{def}}{=} \left\{ \boldsymbol{\xi}_{\mathcal{H}} \in [C^0(\Sigma^{n-1})]^3 \ : \ \boldsymbol{\xi}_{\mathcal{H}} = \boldsymbol{\chi}_{\mathcal{H}} \circ \left(\boldsymbol{\psi}_{\mathcal{H}}^{n-1}\right)^{-1}, \quad \boldsymbol{\chi}_{\mathcal{H}} \in [X_{\mathcal{H}}^{\Sigma}]^3 \right\}. \tag{19}$$

Note that the discrete Lagrange multiplier space $\boldsymbol{\Lambda}_{\mathcal{H}}^n$ is the standard continuous piece-wise affine finite element space onto the deformed interface $\Sigma^{n-1} = \boldsymbol{\psi}_{\mathcal{H}}^{n-1}(\Sigma)$ at the previous time level.

For the definition of the discrete pressure space, we need to introduce a few more notations. We let $\Omega_i^{n-1} \subset \Omega$ denote the i-th fluid subdomain in each side of the interface at the previous time level, with $i = 1, 2$. If Σ^{n-1} does not fully split Ω into two subdomains, we introduce a fictitious interface $\Sigma_{\mathrm{fic}}^{n-1}$, closing Σ^{n-1}, as illustrated in Figure 3. Note

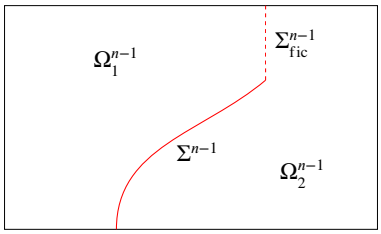

Figure 3: Example of an open configuration with the fictitious interface $\Sigma_{\mathrm{fic}}^{n-1}$.

that the purpose of $\Sigma_{\mathrm{fic}}^{n-1}$ is simply to facilitate the definition of Ω_i^{n-1}. A detailed rationale of the choice and construction of this fictitious interface is provided for each numerical example of Section 4. The discrete pressure space at time level n is defined as:

$$Q_h^n \overset{\text{def}}{=} \widetilde{Q}_h \oplus \langle 1_{\Omega_1^{n-1}} \rangle \subset Q, \quad \widetilde{Q}_h \overset{\text{def}}{=} X_h^{\mathrm{f}} \subset Q, \tag{20}$$

where the symbol $1_{\Omega_1^{n-1}}$ denotes the characteristic function of Ω_1^{n-1} and $\langle 1_{\Omega_1^{n-1}} \rangle$ the vector space spanned by $1_{\Omega_1^{n-1}}$. Note that, in contrast to [27], the discrete pressure Q_h^n is time dependent, due to the dynamic nature of the interface. Each discrete pressure $q_h \in Q_h^n$ can hence be decomposed into the sum of two contributions, namely,

$$q_h = \widetilde{q}_h + \widehat{q}_h, \tag{21}$$

where $\widetilde{q}_h \in \widetilde{Q}_h$ is a continuous piecewise affine function over the whole computational domain Ω, and $\widehat{q}_h \in \langle 1_{\Omega_1^{n-1}} \rangle$ is a Heaviside function that allows strong discontinuities across the interface Σ^{n-1}. Moreover, the following relations hold

$$\widehat{q}_h = [\![q_h]\!] 1_{\Omega_1^{n-1}}, \quad \widetilde{q}_h = q_h - [\![q_h]\!] 1_{\Omega_1^{n-1}}, \tag{22}$$

where $[\![q_h]\!]$ is simply the constant jump of q_h across Σ^{n-1}. As outlined in [27], the continuous part $\widetilde{q}_h$ of the discrete pressures q_h only guarantees global mass conservation in Ω. The purpose of the Heaviside part $\widehat{q}_h$ is precisely to enhance interfacial mass conservation across Σ^{n-1} by simply enforcing global mass conservation on the fluid subdomain Ω_1^{n-1}. It should be noted that the choice of Ω_1^{n-1} and Ω_2^{n-1} is arbitrary, so that the characteristic function could have been taken over Ω_2^{n-1} instead.

The fully discrete approximation of the fluid subproblem (11) reads as follows: Find $\left(\boldsymbol{u}_h^n, p_h^n, \boldsymbol{\lambda}_{\mathcal{H}}^n\right) \in \boldsymbol{V}_h \times Q_h^n \times \boldsymbol{\Lambda}_{\mathcal{H}}^n$ such that

$$\rho^{\mathrm{f}} \int_\Omega \partial_\tau \boldsymbol{u}_h^n \cdot \boldsymbol{v}_h + a_h^{\mathrm{f}}\left(\boldsymbol{u}_h^{n-1}; (\boldsymbol{u}_h^n, p_h^n), (\boldsymbol{v}_h, q_h)\right) - \int_{\Sigma^{n-1}} \boldsymbol{\lambda}_{\mathcal{H}}^n \cdot \boldsymbol{v}_h + \int_{\Sigma^{n-1}} \boldsymbol{\xi}_{\mathcal{H}} \cdot \left(\boldsymbol{u}_h - \boldsymbol{u}_{\mathcal{H}}^{\mathrm{s},n-1/2} \circ \left(\boldsymbol{\psi}_{\mathcal{H}}^{n-1}\right)^{-1}\right) + s_h^{\mathrm{BH},n-1}\left(\left([\![p_h^n]\!], \boldsymbol{\lambda}_{\mathcal{H}}^n\right), \left([\![q_h]\!], \boldsymbol{\xi}_{\mathcal{H}}\right)\right) = 0 \tag{23}$$

for all $\left(\boldsymbol{v}_h, q_h, \boldsymbol{\xi}_{\mathcal{H}}\right) \in \boldsymbol{V}_h \times Q_h^n \times \boldsymbol{\Lambda}_{\mathcal{H}}^n$. Here, the fluid discrete form a_h^{f} is given by

$$a_h^{\mathrm{f}}\left(\boldsymbol{z}_h;(\boldsymbol{u}_h,p_h),(\boldsymbol{v}_h,q_h)\right) \overset{\text{def}}{=} a^{\mathrm{f}}\left(\boldsymbol{z}_h;(\boldsymbol{u}_h,p_h),(\boldsymbol{v}_h,q_h)\right) + \frac{\rho^{\mathrm{f}}}{2}\int_\Omega (\boldsymbol{\nabla}\cdot\boldsymbol{z}_h)\boldsymbol{u}_h\cdot\boldsymbol{v}_h + s_h^{\mathrm{SP}}\left(\boldsymbol{z}_h;(\boldsymbol{u}_h,\widetilde{p}_h),(\boldsymbol{v}_h,\widetilde{q}_h)\right),$$

where the second and third terms correspond to the Temam's trick and to the SUPG/PSPG stabilization operator, respectively, that is,

$$s_h^{\mathrm{SP}}\left(\boldsymbol{z}_h;(\boldsymbol{u}_h,\widetilde{p}_h),(\boldsymbol{v}_h,\widetilde{q}_h)\right) \overset{\text{def}}{=} \sum_{K\in\mathcal{T}_h^\Omega}\int_K \delta_h\left(\rho^{\mathrm{f}}\left(\boldsymbol{z}_h\cdot\nabla\right)\boldsymbol{u}_h + \nabla\widetilde{p}_h\right)\cdot\left(\rho^{\mathrm{f}}\left(\boldsymbol{z}_h\cdot\nabla\right)\boldsymbol{v}_h + \nabla\widetilde{q}_h\right), \tag{24}$$

with

$$\delta_h \overset{\text{def}}{=} \frac{\gamma_{\mathrm{SP}}\rho^{\mathrm{f}}}{\sqrt{\frac{4}{\tau^2}+\frac{16\mu^2}{h^4(\rho^{\mathrm{f}})^2}+\frac{4|\boldsymbol{z}_h|^2}{h^2}}}$$

and where $\gamma_{\mathrm{SP}} > 0$ is the stabilization parameter. The purpose of (24) is twofold: to overcome the lack of inf-sup compatibility between the velocity and pressure spaces $\boldsymbol{V}_h$ and Q_h^n, and to guarantee robustness for high local Reynolds numbers (see, e.g., [76]). Note that the pressure stabilization only acts on the continuous part of the discrete pressures, which is enough for stability (see [27]).

Finally, the last term in (23) is a weakly consistent Lagrange multiplier stabilization which serves to overcome the potential lack of inf-sup stability between the spaces $\boldsymbol{V}_h$ and $\boldsymbol{\Lambda}_{\mathcal{H}}^n$. By building on [27], this term takes the form

$$s_h^{\mathrm{BH},n-1}\left(\left(\eta,\lambda_{\mathcal{H}}\right),\left(\chi,\boldsymbol{\xi}_{\mathcal{H}}\right)\right) \overset{\text{def}}{=} \frac{h}{\gamma_\lambda\mu}\int_{\Sigma^{n-1}}\left(\lambda_{\mathcal{H}}+\eta\boldsymbol{n}_{\Sigma^{n-1}}\right)\cdot\left(\boldsymbol{\xi}_{\mathcal{H}}+\chi\boldsymbol{n}_{\Sigma^{n-1}}\right), \tag{25}$$

where $\gamma_\lambda > 0$ is a user-defined dimensionless parameter. A salient feature of (25) is that it vanishes for interfacial stress jumps that reduce to a constant pressure, i.e., $\boldsymbol{\lambda} = -c\boldsymbol{n}_\Sigma$, with $c \in \mathbb{R}$. This provides superior consistency with respect to standard Lagrange multiplier stabilizations in the context of fictitious domain methods (see, e.g., [6]).

Now, by taking $(\boldsymbol{v}_h, \boldsymbol{\xi}_{\mathcal{H}}) = (\boldsymbol{0},\boldsymbol{0})$ in (23), one gets the following discrete continuity equation

$$\int_\Omega q_h\boldsymbol{\nabla}\cdot\boldsymbol{v}_h + s_h^{\mathrm{SP}}\left(\boldsymbol{u}_h^{n-1};(\boldsymbol{u}_h^n,\widetilde{p}_h^n),(\boldsymbol{0},\widetilde{q}_h)\right) + s_h^{\mathrm{BH},n-1}\left(\left(\llbracket p_h^n\rrbracket,\boldsymbol{\lambda}_{\mathcal{H}}^n\right),\left(\llbracket q_h\rrbracket,\boldsymbol{0}\right)\right) = 0 \tag{26}$$

for all $q_h \in Q_h^n$. Yet, using (22), (22) and (25), we equivalently have

$$\begin{aligned}
&\int_\Omega \widetilde{q}_h\boldsymbol{\nabla}\cdot\boldsymbol{v}_h + s_h^{\mathrm{SP}}\left(\boldsymbol{u}_h^{n-1};(\boldsymbol{u}_h^n,\widetilde{p}_h^n),(\boldsymbol{0},\widetilde{q}_h)\right) = 0,\\
&\chi\left(\int_{\partial\Omega_1^{n-1}}\boldsymbol{u}_h^n\cdot\boldsymbol{n} + \frac{h}{\gamma_\lambda\mu}\int_{\Sigma^{n-1}}\left(\boldsymbol{\lambda}_{\mathcal{H}}{}^n\cdot\boldsymbol{n}_{\Sigma^{n-1}} + \llbracket p_h^n\rrbracket\right)\right) = 0
\end{aligned} \tag{27}$$

for all $\widetilde{q}_h \in \widetilde{Q}_h$ and $\chi = \llbracket q_h\rrbracket \in \mathbb{R}$. By testing $(27)_1$ with $\widetilde{q}_h = 1$, and after integration by parts in the first term, we get global mass conservation in Ω, i.e.,

$$\int_{\partial\Omega}\boldsymbol{u}_h^n\cdot\boldsymbol{n} = 0.$$

Unfortunately, this does not prevent spurious leakage across Σ^{n-1}. The purpose of $(27)_2$ is precisely to enhance interfacial mass conservation by weakly enforcing global mass conservation in the subdomain Ω_1^{n-1}. Note that this is a direct consequence of the discontinuous nature of the discrete pressures in $q_h \in Q_h^n$ across $\Sigma^{n-1} \cup \Sigma_{\mathrm{fic}}^{n-1}$, which involve the additional degree of freedom $\llbracket q_h\rrbracket$.

The aforementioned explicit treatment of the geometrical non-linearity appears in (23) through the interface integrals over Σ^{n-1} and the composition with the inverse of the deformation map $\boldsymbol{\psi}_{\mathcal{H}}^{n-1}$. The interface terms $\int_{\Sigma^{n-1}}\boldsymbol{\lambda}_{\mathcal{H}}^n\cdot\boldsymbol{v}_h$ and $\int_{\Sigma^{n-1}}\boldsymbol{\xi}_{\mathcal{H}}\cdot\boldsymbol{u}_h$ deserve special attention, as they involve integrals of discrete functions supported by different unfitted meshes. In the numerical experiments of Section 4, these terms are approximated by a composite quadrature rule over the deformed mid-surface mesh (with 5 Gaussian points per triangle). On the contrary, using the compatibility between the solid discrete space $\boldsymbol{W}_{\mathcal{H}}$ and the Lagrange multiplier space $\boldsymbol{\Lambda}_{\mathcal{H}}^n$, the remaining interface term $\int_{\Sigma^{n-1}}\boldsymbol{\xi}_{\mathcal{H}}\cdot\boldsymbol{u}_{\mathcal{H}}^{\mathrm{s},n-1/2}\circ\left(\boldsymbol{\psi}_{\mathcal{H}}^{n-1}\right)^{-1}$ (and also the last term of (15)) yields a simple interfacial mass matrix.

3.3. Numerical method

The proposed fully discrete approximation of the fluid-structure interaction problem (10) is obtained by collecting the relations (15), (16) and (23). From the computational point of view, it is worth noting that the discontinuous part of the pressure in (23) requires the integration over cut elements. This is a direct consequence of the fact that fluid mesh $\mathcal{T}_h^{\Omega}$ is not fitted to Ω_1^{n-1}. Nevertheless, owing to (26) and (27), the fluid sub-problem (23) can be formulated as the standard continuous piece-wise affine approximation with the additional single degree of freedom $[\![q_h]\!]$ for the pressure. Note that this only involves surface integrals over Σ^{n-1} and $\partial\Omega_1^{n-1}$, thereby avoiding cut elements. The resulting numerical method is detailed in Algorithm 1.

Algorithm 1 Fictitious domain strongly coupled scheme.

For $n \geq 1$:

1. Find $\left(\boldsymbol{u}_h^n, \widetilde{p}_h^n, \eta^n, \lambda_{\mathcal{H}}^n, \boldsymbol{d}_{\mathcal{H}}^n\right) \in \boldsymbol{V}_h \times \widetilde{Q}_h \times \mathbb{R} \times \boldsymbol{\Lambda}_{\mathcal{H}}^n \times \boldsymbol{W}_{\mathcal{H}}$, with $\boldsymbol{u}_{\mathcal{H}}^{\mathrm{s},n-1/2} = \partial_\tau \boldsymbol{d}_{\mathcal{H}}^n$, such that

$$\begin{cases} \rho^{\mathrm{f}} \displaystyle\int_\Omega \partial_\tau \boldsymbol{u}_h^n \cdot \boldsymbol{v}_h + a_h^{\mathrm{f}}\left(\boldsymbol{u}_h^{n-1}; (\boldsymbol{u}_h^n, \widetilde{p}_h^n), (\boldsymbol{v}_h, \widetilde{q}_h)\right) \\ \quad - \eta^n \displaystyle\int_{\partial\Omega_1^{n-1}} \boldsymbol{v}_h \cdot \boldsymbol{n} + \chi \int_{\partial\Omega_1^{n-1}} \boldsymbol{u}_h^n \cdot \boldsymbol{n} \\ \quad - \displaystyle\int_{\Sigma^{n-1}} \lambda_{\mathcal{H}}^n \cdot \boldsymbol{v}_h + \int_{\Sigma^{n-1}} \boldsymbol{\xi}_{\mathcal{H}} \cdot \left(\boldsymbol{u}_h - \boldsymbol{u}_{\mathcal{H}}^{\mathrm{s},n-1/2} \circ \left(\boldsymbol{\psi}_{\mathcal{H}}^{n-1}\right)^{-1}\right) \\ \quad + s_h^{\mathrm{BH},n}\left((\eta^n, \lambda_{\mathcal{H}}^n), (\chi, \boldsymbol{\xi}_{\mathcal{H}})\right) = 0, \end{cases} \tag{28}$$

$$\rho^{\mathrm{s}}\left(\partial_\tau \boldsymbol{u}_{\mathcal{H}}^{\mathrm{s},n}, \boldsymbol{\xi}_{\mathcal{H}}\right)_{\mathrm{s}} + a_{\mathcal{H}}^{\mathrm{s}}\left(\boldsymbol{d}_{\mathcal{H}}^{n-1/2}; \boldsymbol{\xi}_{\mathcal{H}}\right) = -\int_{\Sigma^{n-1}} \lambda_{\mathcal{H}}^n \cdot \boldsymbol{w}_{\mathcal{H}} \circ \left(\boldsymbol{\psi}_{\mathcal{H}}^{n-1}\right)^{-1} \tag{29}$$

   for all $\left(\boldsymbol{v}_h, \widetilde{q}_h, \chi, \boldsymbol{\xi}_{\mathcal{H}}, \boldsymbol{w}_{\mathcal{H}}\right) \in \boldsymbol{V}_h \times \widetilde{Q}_h \times \mathbb{R} \times \boldsymbol{\Lambda}_{\mathcal{H}}^n \times \boldsymbol{W}_{\mathcal{H}}$.

2. Interface update:

$$\boldsymbol{\psi}_{\mathcal{H}}^n = \boldsymbol{I}_\Sigma + \boldsymbol{d}_{\mathcal{H}}^n \quad \text{on} \quad \Sigma, \qquad \Sigma^n = \boldsymbol{\psi}_{\mathcal{H}}^n(\Sigma).$$

The relation $(28)_2$ in the fluid subproblem enforces the enhanced interfacial mass conservation. Note also that the fluid and solid subproblems (28) and (29) are fully coupled. In what follows, this strongly coupling is solved by using a partitioned solution procedure based on interface Newton-GMRES Dirichlet–Neumann iterations (see, e.g., [32, 29]).

4. Numerical examples

The purpose of this section is to provide a comprehensive numerical illustration of the capabilities of Algorithm 1 in three different scenarios. Section 4.1 provides numerical evidence of the accuracy of Algorithm 1 with respect to well-established methods reported in the literature. To this purpose, we consider a series of 2D immersed FSI benchmarks. In Section 4.2, we compare the approximations provided by Algorithm 1 in both the case of the 2D- and 3D-shell models. Finally, Section 4.3 presents the application of Algorithm 1 to the simulation of the dynamics of the aortic valve where, in particular, we investigate the benefits of the additional mass constraint in the fluid. Throughout the following sections, unless explicitly mentioned, all physical quantities and parameters are expressed in the centimeter-gram-second (CGS) unit system.

4.1. Comparative study

In this section, the accuracy of Algorithm 1 is assessed through comparisons with the following alternative finite-element-based FD methods:

- FD-PE: the standard FD method with penalty and continuous piecewise affine approximations (e.g., [70, 31, 3, 16]). This is basically Algorithm 1 without the terms involving η^n and χ, and with a penalized kinematic constraint instead of the Lagrange multiplier terms in $\lambda_{\mathcal{H}}^n$ and $\boldsymbol{\xi}_{\mathcal{H}}$;

- FD-GD: the previous method with a grav-div penalty term in the vicinity of the interface, to enhance mass conservation (e.g., [47, 34, 20, 16]);
- NXFEM: the Nitsche-XFEM method (e.g., [2, 17, 87, 16]), which involves a cut-FEM approach and allows for discrete weak (velocity) and strong (pressure) interfacial discontinuities through overlapping meshes.

Furthermore, a fitted mesh Arbitrary Lagrangian-Eulerian (ALE) method, using highly resolved space–time grids, is used as reference in the comparisons.

The accuracy of the methods is assessed using three successive space-time refinement levels: *M1*, *M2*, and *M3*. These levels correspond to uniform refinements of *M1*, with refinement factors of 2 and 4 in both the spatial and temporal directions. Specifically, the spatial grids consist of uniform structured meshes, as illustrated in Figure 4. Detailed descriptions of these refinement levels are provided subsequently for each numerical example. In all test-

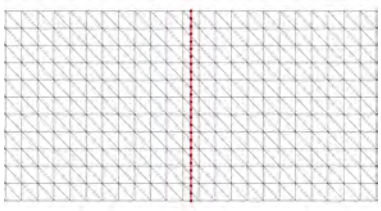

Figure 4: Example of computational meshes used in the comparative study of Section 4.1. The fluid mesh is represented in gray, while the structure mesh is shown in red.

cases, the solid is described by a nonlinear Timoshenko curved beam model, discretized with linear MITC elements (see, e.g., [7, 64, 56]).

Consistent parameter settings are employed across all test cases. The NXFEM method uses $\gamma_{\mathrm{v}} = \gamma_{\mathrm{p}} = 0.01$ for CIP stabilization, $\gamma_{\mathrm{g}} = 1$ for ghost penalty, and $\gamma = 100$ for Nitsche's penalty. Both the FD-PE and FD-GD methods share a common penalty parameter ϵ, with the FD-PE method employing $\gamma_{\mathrm{SP}} = 1$ (SUPG/PSPG stabilization), while the FD-GD method combines $\gamma_{\mathrm{SP}} = 1$ globally, enhanced to $\gamma_{\mathrm{SP}} = \gamma_{\mathrm{gd}}$ near the interface and $\gamma_{\mathrm{d}} = 1$ (grad-div penalty). Additional parameter details are provided subsequently for numerical examples. All the numerical simulations of the present section have been performed with the `FELiScE` finite element library[1].

4.1.1. Idealized closed valve

As a first example, we consider a benchmark problem mimicking the behavior of a closed valve subjected to a pressure gradient (see, e.g., [47, 78]). The problem consists in an elastic beam clamped at its extremities and immersed in a channel filled with an incompressible Newtonian fluid. The fluid domain is given by $\Omega = (0, 4) \times (0, 1)$, while the reference solid configuration is given by $\Sigma = \{2\} \times (0, 1)$ (see Figure 5). The time domain spans $t \in [0, 3]$, representing the duration required for the system to reach a steady state from its initial rest state.

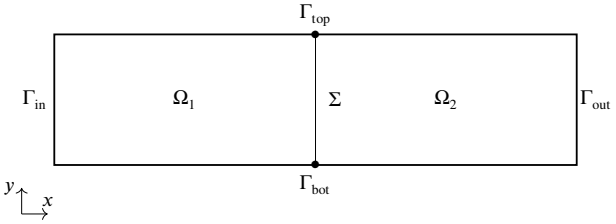

Figure 5: Idealized closed valve geometric configuration.

Regarding the boundary conditions of the fluid, no-slip is enforced on $\Gamma_{\mathrm{bot}} \cup \Gamma_{\mathrm{top}}$, whereas zero traction is enforced on the lateral boundary Γ_{out}. On the inlet boundary Γ_{in}, a time-dependent traction force is applied as $\boldsymbol{\sigma}^{\mathrm{f}}(\boldsymbol{u}, p) = -p_{\mathrm{in}}\boldsymbol{n}$, with the inlet pressure given by $p_{in}(t) = 3 \cdot 10^5 \operatorname{atanh}(10\,t)$. The physical parameters of the fluid are set to $\rho^{\mathrm{f}} = 100$ and $\mu = 10$, while for the solid we have $\rho^{\mathrm{s}} = 100$, $\epsilon = 0.0212$, $E = 5.6 \cdot 10^7$ and $\nu = 0.4$.

[1] `https://gitlab.inria.fr/felisce/felisce`

	Number of elements		Time-step length
	Fluid mesh	Solid mesh	
ALE	25600	80	$2.5 \cdot 10^{-4}$
M1	1034	24	$2 \cdot 10^{-3}$
M2	4370	50	$1 \cdot 10^{-3}$
M3	17954	100	$5 \cdot 10^{-4}$

Table 1
Idealized closed valve space-time grids details.

Spatial and temporal discretization. Table 1 provides details regarding the space-time grid used for the ALE method, as well as the three refinement levels (*M1*, *M2*, and *M3*) employed for the unfitted mesh methods.

Additionally, across all refinement levels, the parameters ϵ and γ_{gd} for the FD-PE and FD-GD methods are set to 10^{-5} and 10^{-4}, respectively. For a detailed and comprehensive discussion about the value of the parameter γ_{gd}, we refer to [16, Section 4.2.3]. The parameter γ_λ for Algorithm 1 is set to 10 for all the refinement levels. Additionally, since the interface Σ^{n-1} divides the domain Ω into two subdomains, Ω_1^{n-1} and Ω_2^{n-1}, at each time step (see, e.g., Figure 5 for $n = 0$), the fictitious interface is not needed for the definition of the pressure space Q_h^n in (20).

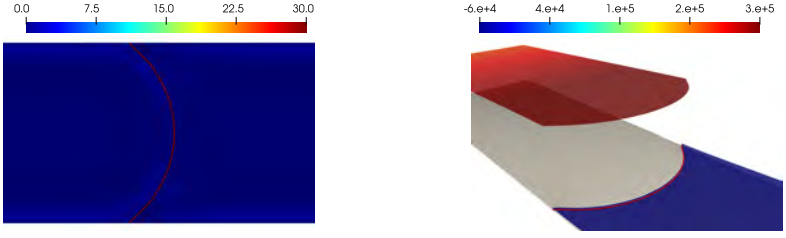

(a) Velocity magnitude (reference). (b) Pressure (reference).

Figure 6: Snapshots of the velocity magnitude and pressure at $t = 0.125$ for the reference solution.

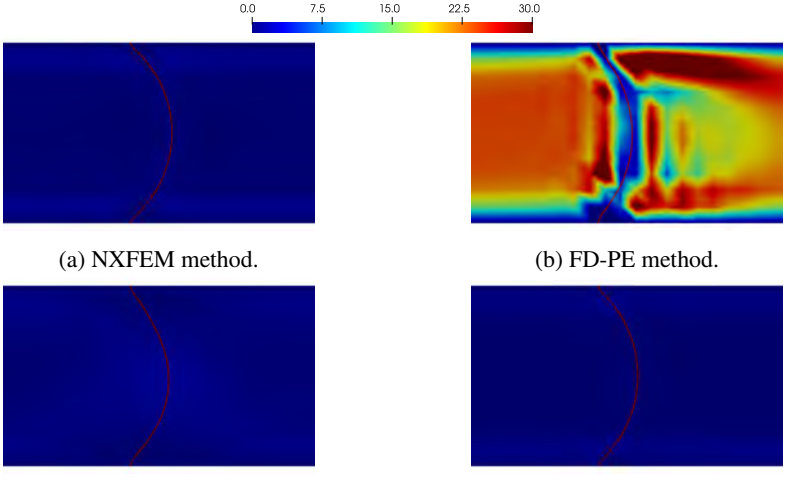

(a) NXFEM method. (b) FD-PE method.

(c) FD-GD method. (d) Algorithm 1.

Figure 7: Snapshots of the fluid velocity magnitude at $t = 0.125$ for the *M1* refinement level.

Comparison of the results. Once the inlet pressure is prescribed, the elastic solid initiates its deformation, leading to bending and elongation. After a brief initial transition phase, the system gradually reaches a steady state characterized

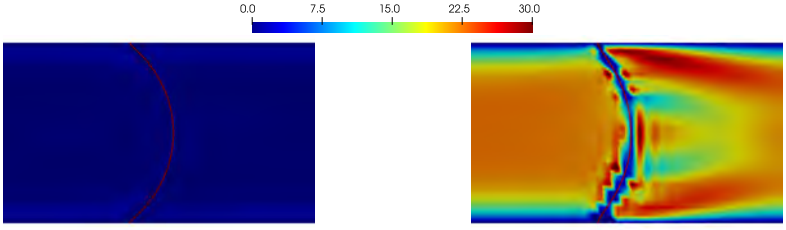

(a) NXFEM method. (b) FD-PE method.

(c) FD-GD method. (d) Algorithm 1.

Figure 8: Snapshots of the fluid velocity magnitude at $t = 0.125$ for the *M2* refinement level.

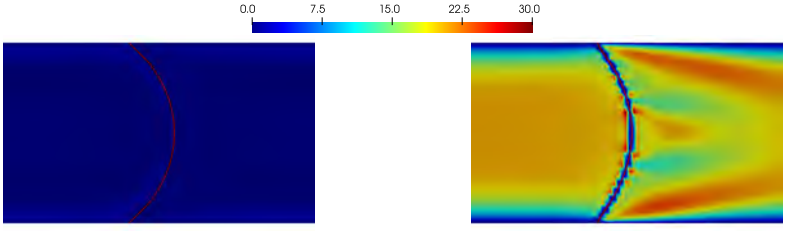

(a) NXFEM method. (b) FD-PE method.

(c) FD-GD method. (d) Algorithm 1.

Figure 9: Snapshots of the fluid velocity magnitude at $t = 0.125$ for the *M3* refinement level.

by a constant pressure jump across the interface. In this state, both the fluid and solid velocities are negligible, and the pressure becomes a piecewise constant function. Specifically, it takes the values of 3×10^5 on one side of the interface and zero on the other side. For comparison purposes, we consider the results at $t = 0.125$.

Figure 6 shows the reference solution obtained using the fitted mesh ALE method, while Figures 7–12 report the velocity magnitude and pressure fields obtained with Algorithm 1 and the three alternative finite-element-based FD methods. From these results, it is evident that regardless of the refinement level, the FD-PE method yields a spurious velocity field within the channel (see Figures 7b, 8b, 9b) and, consequently, a significantly underestimated pressure in comparison to the reference solution, see Figures 6b, 10b, 11b, 12b. This is a well-known limitation of the FD-PE method with continuous pressure approximations (see, e.g., [4, 47]). Although global mass conservation in the whole domain Ω is ensured, the continuous nature of the pressure approximation does not guarantee mass conservation across the interface. This limitation is effectively resolved by the other unfitted mesh methods. Algorithm 1 overcomes this issue through the additional pressure basis function, which, as discussed in Section 3.2, enables the accurate representation of the pressure discontinuity across the interface (see Figures 10d, 11d, and 12d). Consequently, it enhances interfacial mass conservation and yields a velocity field free from parasitic flows (see Figures 7d, 8d, and

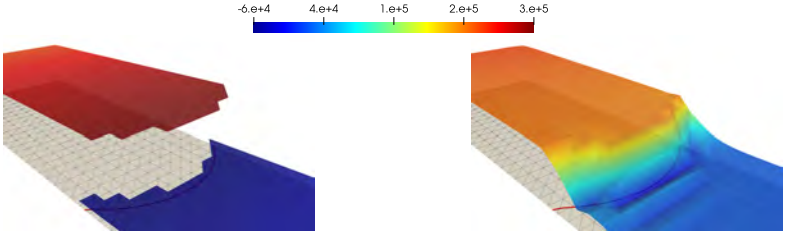

(a) NXFEM method. (b) FD-PE method.

(c) FD-GD method. (d) Algorithm 1.

Figure 10: Snapshots of the fluid pressure at $t = 0.125$ for the *M1* refinement level.

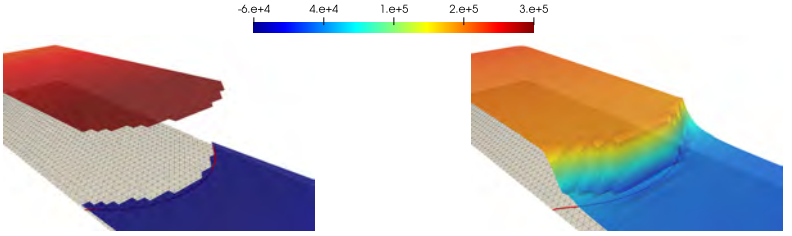

(a) NXFEM method. (b) FD-PE method.

(c) FD-GD method. (d) Algorithm 1.

Figure 11: Snapshots of the fluid pressure at $t = 0.125$ for the *M2* refinement level.

9d). Similarly, the NXFEM method correctly retrieves the velocity and pressure fields. Indeed, the strong discontinuity of the discrete pressure also guarantees interfacial mass conservation. This is clearly illustrated in Figures 7a, 8a, 9a and Figures 10a, 11a, 12a for velocity and pressure, respectively. Furthermore, the comparisons also show that as expected the FD-GD method removes the spurious velocity field of the FD-PE method. Indeed, the grad-div penalty term enhances local mass conservation in the vicinity of the interface (see, e.g., [47]), and thus significantly reduces interfacial mass leakage, as shown in Figures 7c, 8c, 9c. The pressure field also shows very good agreement with respect to the reference solution, as can be inferred from Figures 10c, 11c, 12c.

Figure 13 provides a comparison of the evolution of the horizontal displacement at the interface mid-point. The NXFEM and FD-GD methods and Algorithm 1 show a better agreement with the reference solution than the FD-PE method. In particular, unlike the other methods, the FD-PE method fails to capture the dynamics of the structure. Similar results can be inferred from Table 2, which reports the relative mid-point displacement L^2-errors for Algorithm 1 and the alternative unfitted-mesh approaches, evaluated with respect to the reference ALE solution over the entire time interval. The results confirm the qualitative trends observed in Figure 13: the NXFEM method yields the highest accuracy, while Algorithm 1 attains competitive performance, also comparable to the FD-GD approach. In contrast,

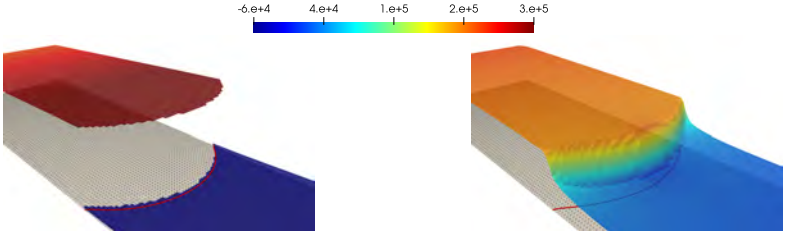

(a) NXFEM method. (b) FD-PE method.

(c) FD-GD method. (d) Algorithm 1.

Figure 12: Snapshots of the fluid pressure at $t = 0.125$ for the *M3* refinement level.

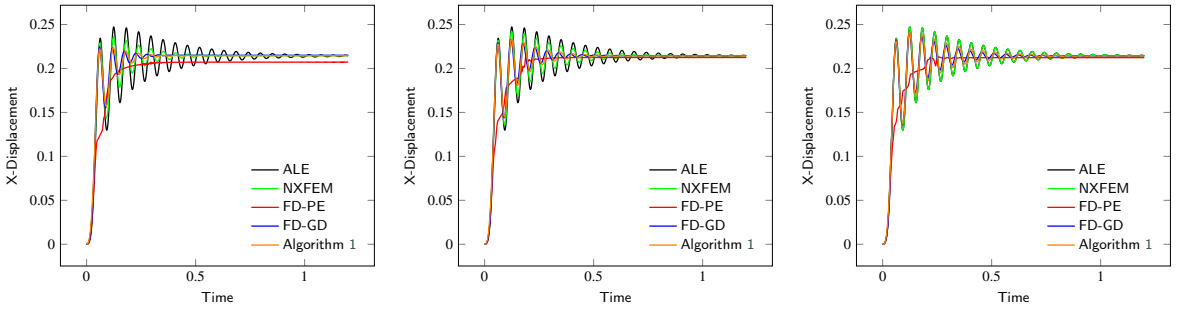

(a) *M1* vs. Reference. (b) *M2* vs. Reference. (c) *M3* vs. Reference.

Figure 13: Time history of the x-displacement of the solid mid-point.

	NXFEM	FD-PE	FD-GD	Algorithm 1
M1	$2.01 \cdot 10^{-2}$	$6.58 \cdot 10^{-2}$	$3.80 \cdot 10^{-2}$	$3.10 \cdot 10^{-2}$
M2	$1.05 \cdot 10^{-2}$	$5.45 \cdot 10^{-2}$	$2.75 \cdot 10^{-2}$	$2.20 \cdot 10^{-2}$
M3	$1.04 \cdot 10^{-3}$	$5.43 \cdot 10^{-2}$	$1.75 \cdot 10^{-2}$	$1.21 \cdot 10^{-2}$

Table 2
Relative L^2 displacement errors of the solid mid-point displacement for the different FD methods.

the FD-PE method consistently yields the largest errors across all refinement levels, highlighting its limited capability to accurately capture the dynamics of the solid. Moreover, Algorithm 1 shows a systematic error reduction as the mesh is refined from *M1* to *M3*, confirming its convergence properties alongside the other established methods.

4.1.2. Idealized open valve

As a second example, we consider the benchmark problem proposed in previous studies [37, 44, 47, 82], which focuses on simulating the behavior of an idealized heart valve in 2D. The 2D valve consists of two identical cantilevered elastic beams attached to the walls of a channel filled with an incompressible Newtonian fluid. The initial geometric configuration is illustrated in Figure 14.

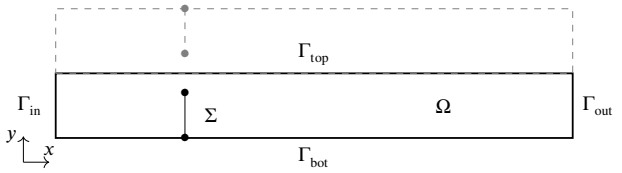

Figure 14: Idealized open valve geometric configuration.

Due to the symmetry of the problem, simulations are performed on half of the domain, incorporating appropriate symmetry boundary conditions. The fluid domain is defined as $\Omega = (0, 8)\times(0, 0.805)$, while the reference configuration of the solid is $\Sigma = \{2\} \times (0, 0.7)$. The simulation spans a time interval of $[0, 3]$, roughly corresponding to three full cycles of oscillations of the structure. The following conditions are applied on the fluid domain boundaries: a no-slip condition on Γ_{bot}, a symmetry condition on Γ_{top}, and zero traction on the lateral boundary Γ_{out}. Additionally, a parabolic velocity profile is enforced on boundary Γ_{in}, given by: $\boldsymbol{u}(t) = -5y(1.61 - y)\,\mathrm{atanh}(5t)(\sin(2\boldsymbol{\pi}t) + 1.1)\boldsymbol{n}$. The beam is fully clamped at its bottom endpoint. Both the fluid and the solid are initially at rest. The physical parameters for this example are as follows: for the fluid $\rho^{\mathrm{f}} = 100$ and $\mu = 10$, and for the solid $\rho^{\mathrm{s}} = 100$, $\epsilon = 0.0212$, $E = 5.6 \cdot 10^7$ and $\nu = 0.4$.

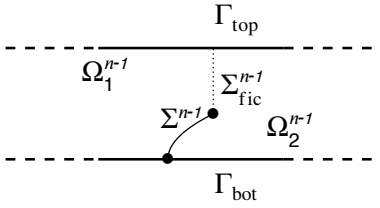

Figure 15: Example of the splitting of the fluid domain Ω into Ω_1^{n-1} and Ω_2^{n-1} using the fictitious interface Σ_{fic}^{n-1}.

Spatial and temporal discretization. Table 3 presents details of the space-time grid used in the ALE method, as well as the configurations for three refinement levels (*M1*, *M2*, and *M3*) in the unfitted mesh methods. In the ALE method, the fluid mesh is refined around the interface. Due to the significant deflection experienced by the interface, the mesh motion is performed using a pseudo-nonlinear elastic extension (see [50]). Regarding the FD-PE and FD-GD methods, the penalty parameter ϵ takes values of 10^{-5}, 10^{-6}, and 10^{-6} for *M1*, *M2*, and *M3*, respectively. The parameter γ_{gd} in the FD-GD method is set to 10^{-4} for all refinement levels. For Algorithm 1, $\gamma_\lambda = 10$. For Algorithm 1, to accurately define the discrete pressure space Q_h^n in (20), we employ the fictitious interface Σ_{fic}^{n-1}, obtained by projecting, at each time step, the endpoint of the structure onto the boundary Γ_{top}, as illustrated in Figure 15.

Comparison of the results. The time-varying velocity profile induces a deformation of the interface, causing it to flex and subsequently return to a position near its initial state, oscillating over time. For comparison purposes, we consider the time instant $t = 0.5$, selected as a representative phase of the oscillation. Figure 16 illustrates the reference solution obtained using the fitted mesh ALE approach. Figures 20b–22b) report the velocity magnitude and pressure fields obtained with Algorithm 1 and the three alternative finite-element-based FD methods. Subsequent refinement further enhances the agreement with the reference solution for all methodologies. Starting from refinement level *M2*, the FD-GD method provides results in close agreement with the reference solution (see Figures 18c and 21c). For the FD-PE approach, the results between *M1* and *M3* clearly illustrates the positive impact of the mesh refinement on the accuracy (see Figures 20b–22b).

Overall, there is a notable agreement in both velocity and pressure fields across all methods for all refinement levels, as it can be inferred from Figures 17–22. In particular, Algorithm 1 and the NXFEM method exhibit a very good agreement with the results of the ALE method from the initial refinement level *M1* (see Figures 17d, 17a, 20d,

	Number of elements		Time-step length
	Fluid mesh	Solid mesh	
ALE	48706	59	$1 \cdot 10^{-3}$
M1	4096	25	$1 \cdot 10^{-2}$
M2	20352	64	$5 \cdot 10^{-3}$
M3	65536	128	$2.5 \cdot 10^{-3}$

Table 3
Idealized open valve space-time grids details.

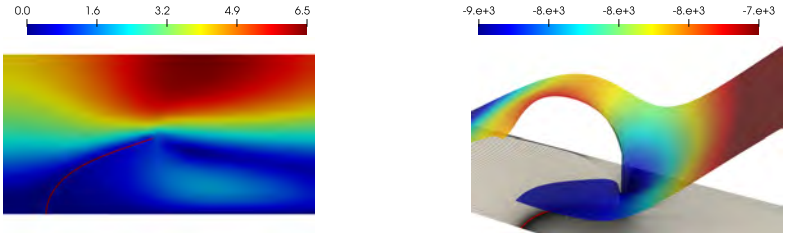

(a) Velocity magnitude (reference). (b) Pressure (reference).

Figure 16: Snapshots of the velocity magnitude and pressure at $t = 0.5$ for the reference solution.

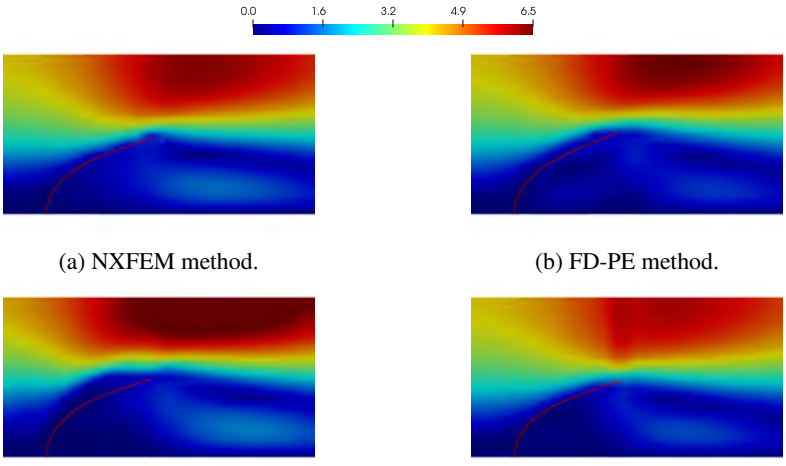

(a) NXFEM method. (b) FD-PE method.

(c) FD-GD method. (d) Algorithm 1.

Figure 17: Snapshots of the fluid velocity magnitude at $t = 0.5$ for the *M1* refinement level.

and 10a). Similar observations can be drawn from Figure 23, which provides a comparison of the temporal evolution of the displacement in the x and y directions of the upper leaflet tip. Both Algorithm 1 and the NXFEM method exhibit good agreement with the ALE method. However, the overall agreement of the FD-GD methods is satisfactory for the *M2* and *M3* refinement levels. Additionally, as mesh refinement increases, the convergence of the FD-PE method solutions towards the reference solution is clearly visible.

Finally, Table 4 presents the relative L^2-errors of the valve top end-point displacement, by comparing the results obtained with Algorithm 1 and the alternative FD methods against the ALE reference solution. As expected, the NXFEM method achieves the highest accuracy, consistent with its optimal convergence properties. Among the other FD methods, Algorithm 1 outperforms both the FD-PE and FD-GD approaches. In particular, the FD-GD method yields large errors at the coarsest refinement level (*M1*), whereas all methods show systematic error reduction under grid refinement.

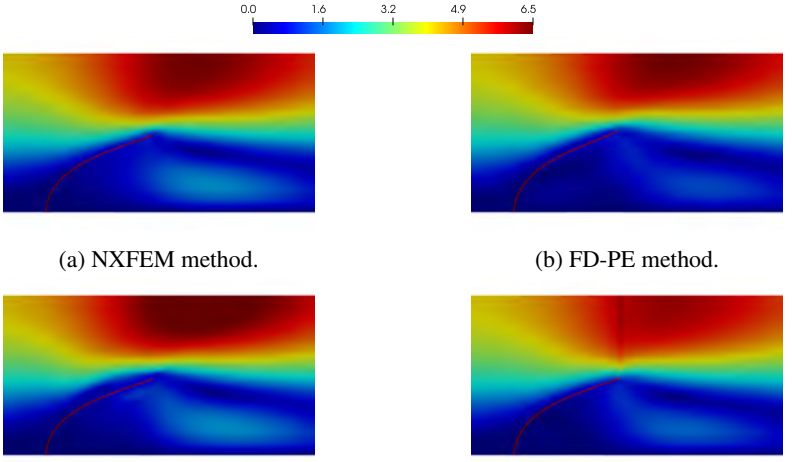

(a) NXFEM method. (b) FD-PE method.

(c) FD-GD method. (d) Algorithm 1.

Figure 18: Snapshots of the fluid velocity magnitude at $t = 0.5$ for the *M2* refinement level.

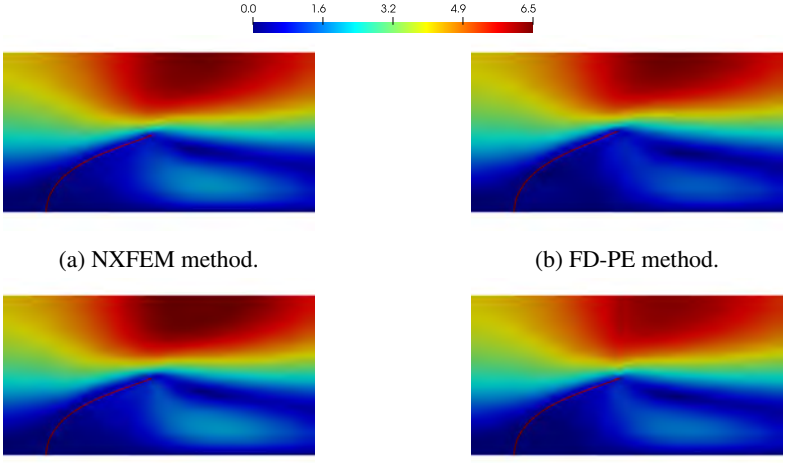

(a) NXFEM method. (b) FD-PE method.

(c) FD-GD method. (d) Algorithm 1.

Figure 19: Snapshots of the fluid velocity magnitude at $t = 0.5$ for the *M3* refinement level.

	NXFEM	FD-PE	FD-GD	Algorithm 1
M1	$2.70 \cdot 10^{-2}$	$6.33 \cdot 10^{-2}$	$9.56 \cdot 10^{-2}$	$2.40 \cdot 10^{-2}$
M2	$1.22 \cdot 10^{-2}$	$5.58 \cdot 10^{-2}$	$3.82 \cdot 10^{-2}$	$1.60 \cdot 10^{-2}$
M3	$7.54 \cdot 10^{-3}$	$4.97 \cdot 10^{-2}$	$1.76 \cdot 10^{-2}$	$1.38 \cdot 10^{-2}$

Table 4
Relative L^2 displacement errors of the solid top end-point displacement for the different FD methods.

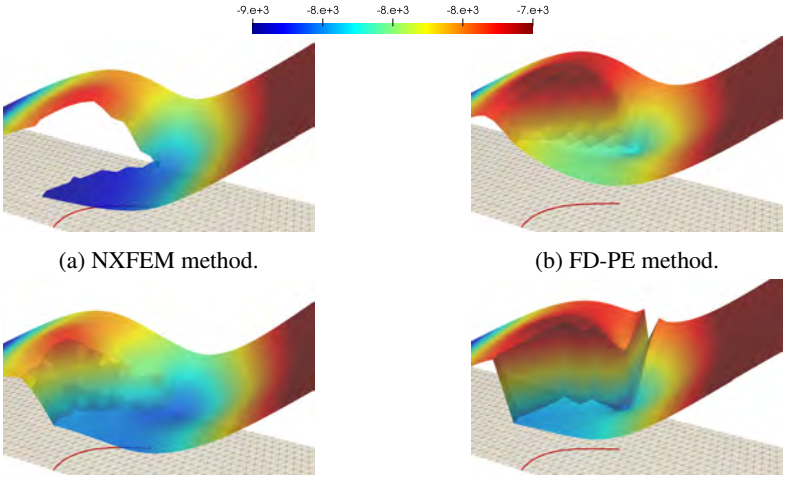

(a) NXFEM method. (b) FD-PE method.

(c) FD-GD method. (d) Algorithm 1.

Figure 20: Snapshots of the fluid pressure at $t = 0.5$ for the *M1* refinement level.

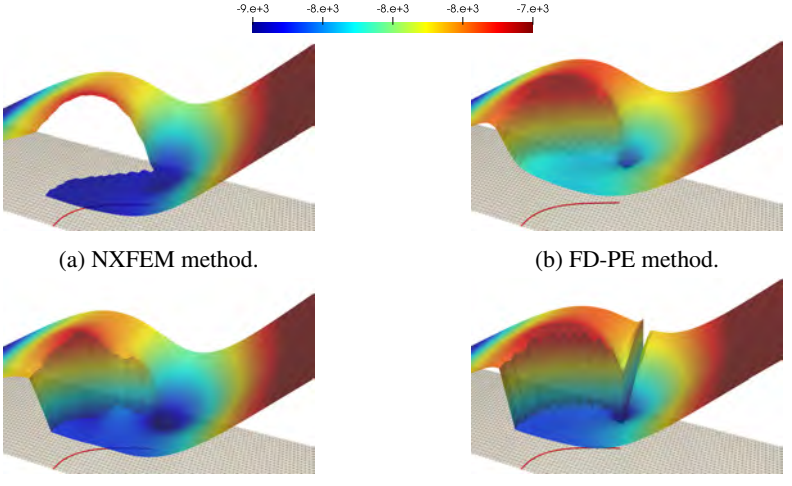

(a) NXFEM method. (b) FD-PE method.

(c) FD-GD method. (d) Algorithm 1.

Figure 21: Snapshots of the fluid pressure at $t = 0.5$ for the *M2* refinement level.

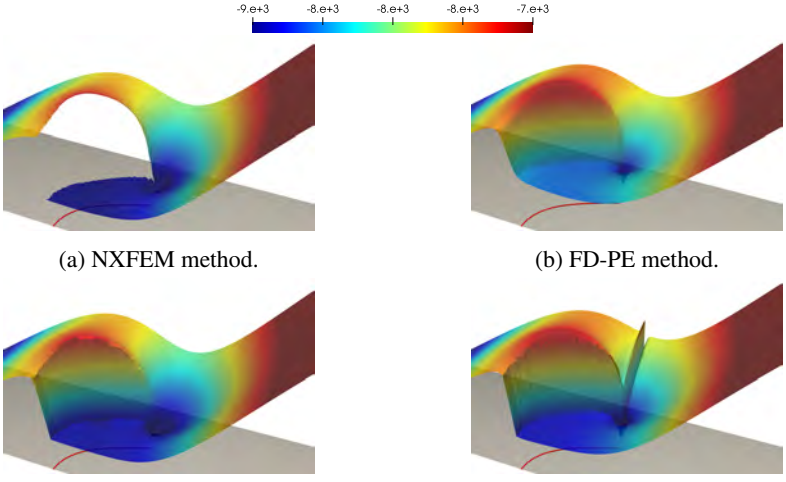

(a) NXFEM method.

(b) FD-PE method.

(c) FD-GD method.

(d) Algorithm 1.

Figure 22: Snapshots of the fluid pressure at $t = 0.5$ for the *M3* refinement level.

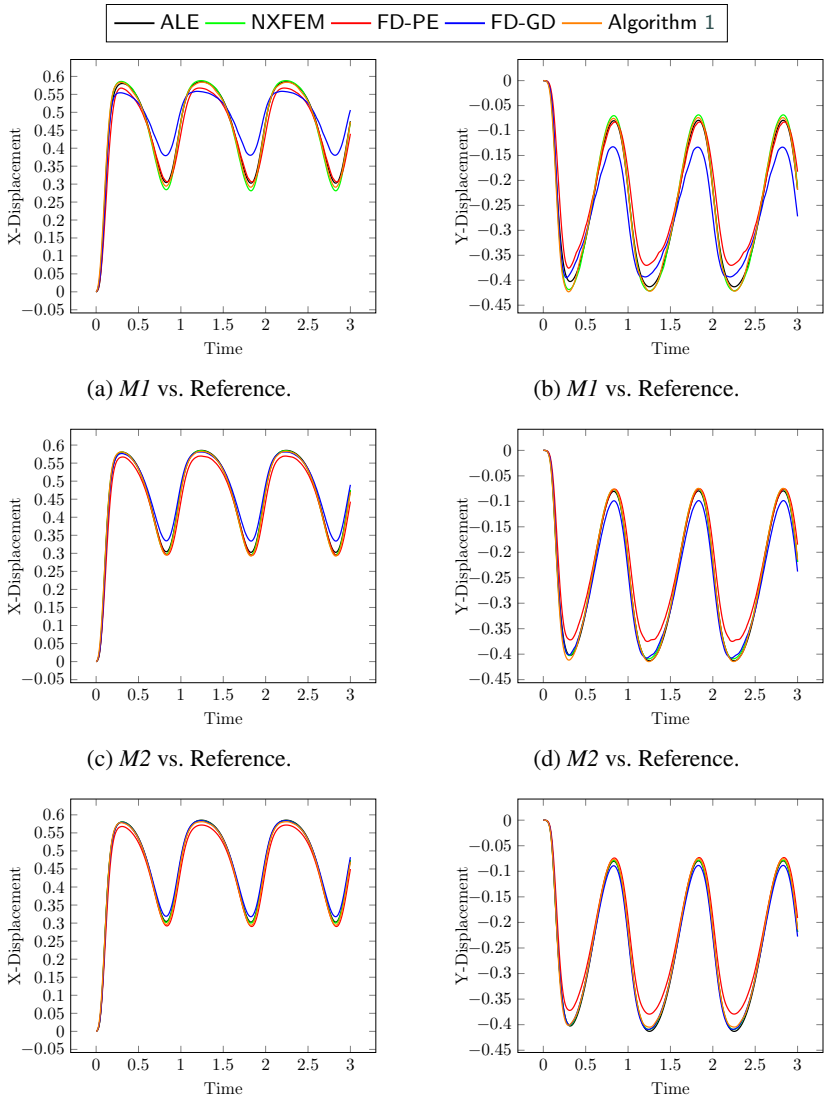

(a) *M1* vs. Reference.

(b) *M1* vs. Reference.

(c) *M2* vs. Reference.

(d) *M2* vs. Reference.

(e) *M3* vs. Reference.

(f) *M3* vs. Reference.

Figure 23: Time history of the x-displacement (left) and y-displacement (right) of the valve end-point.

4.1.3. Vesicle in a lid-driven cavity flow

As last 2D example, we consider a lid-driven cavity with an immersed elastic vesicle (see, e.g., [80, 38, 66, 39]). The fluid domain is defined as the unit square $\Omega = (0,1) \times (0,1)$. The reference configuration of the solid mid-surface Σ is a circle centered at $(0.6, 0.5)$ with a radius of $R = 0.2$. Figure 24 shows the initial geometric configuration. The simulation spans a time interval of 10 s, representing the period required for a complete revolution of the vesicle within Ω. A no-slip boundary condition is enforced on Γ_{wall}, while zero traction is applied to the lateral boundaries Γ_{in} and Γ_{out}. On the upper boundary Γ_{top}, we set $\boldsymbol{u} = (1, 0)$. Initially, both the fluid and the solid are at rest. The physical parameters are chosen as follows: $\rho^{\text{f}} = 100$, $\mu = 10$, $\rho^{\text{s}} = 100$, $\epsilon = 0.0212$, $E = 5.6 \cdot 10^3$ and $\nu = 0.4$.

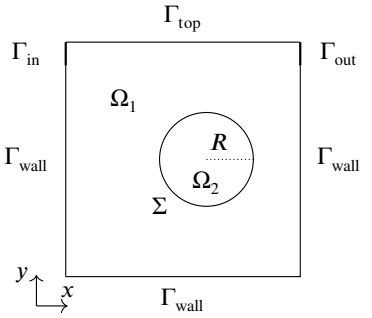

Figure 24: Lid-driven cavity geometric configuration.

Spatial and temporal discretization. Full details on the space-time grids for the fitted mesh ALE method the unfitted mesh methods are given in Table 5. The discrete pressure space Q_h^n for Algorithm 1 is defined by taking Ω_1^{n-1} as the region of the domain Ω lying outside Σ^{n-1} (see Figure 24), so that the fictitious interface is not needed. It is worth noting that the choice of subdomains is arbitrary; selecting the opposite subdomain yields the same result. The penalty parameter ϵ for the FD-PE and FD-GD methods remains constant at $\epsilon = 10^{-4}$ across all refinement levels. Concerning the stabilization parameter γ_{gd}, we set $\gamma_{\text{gd}} = 1$ for *M1*, $\gamma_{\text{gd}} = 10^{-1}$ for *M2*, and $\gamma_{\text{gd}} = 10^{-4}$ for *M3*. Additional details regarding the specific values of the stabilization parameter γ_{gd} can be found in [16, Section 4.3.3]. The parameter γ_λ for Algorithm 1 is set to 10 for all refinement levels.

Comparison of the results. We consider that $t = 4.5$ is the upper limit where we can still refer to the ALE solution as the reference (close to the break-down of the mesh motion procedure, which is performed without remeshing or mesh topology changes, see Figure 25). The corresponding velocity magnitude and pressure fields and vesicle configuration are provided in Figure 26. Figures 27–29 show the snapshots of the fluid velocity magnitude and the vesicle position

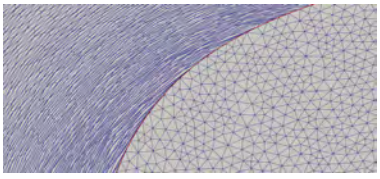

Figure 25: Close-up view of the ALE fluid mesh at time $t = 0.45$. Distortions in the elements lead to the breakdown of the mesh motion procedure.

obtained with the different unfitted mesh methods, at $t = 4.5$ for the different refinement levels. The results for the fluid pressure are given in Figures 30–32.

We observe that Algorithm 1 and the NXFEM method accurately approximate the interface location even with the coarsest refinement levels (see Figures 27a,d–29a,d). These methods also effectively capture the pressure jump between the interior and exterior of the vesicle, with further improvement observed with mesh refinement (see Figures 30a,d–32a,d). The FD-PE method does not show significant pressure jump across the vesicle, regardless of the refinement level used (see Figures 30b, 31b, 32b), resulting in poor interface position approximation (see Figures 27b, 28b, 29b).

	Number of elements		Time-step length
	Fluid mesh	Solid mesh	
ALE	46078	200	$2.5 \cdot 10^{-3}$
M1	800	40	$1 \cdot 10^{-2}$
M2	3200	80	$5 \cdot 10^{-3}$
M3	12800	160	$2.5 \cdot 10^{-3}$

Table 5
Lid-driven cavity space-time grids details.

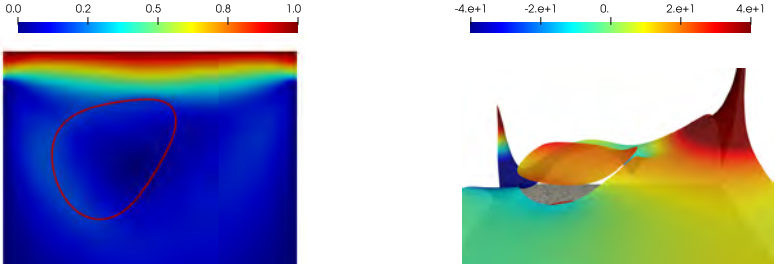

(a) Velocity magnitude (reference). (b) Pressure (reference).

Figure 26: Snapshots of the velocity magnitude and pressure at $t = 4.5$ for the reference solution.

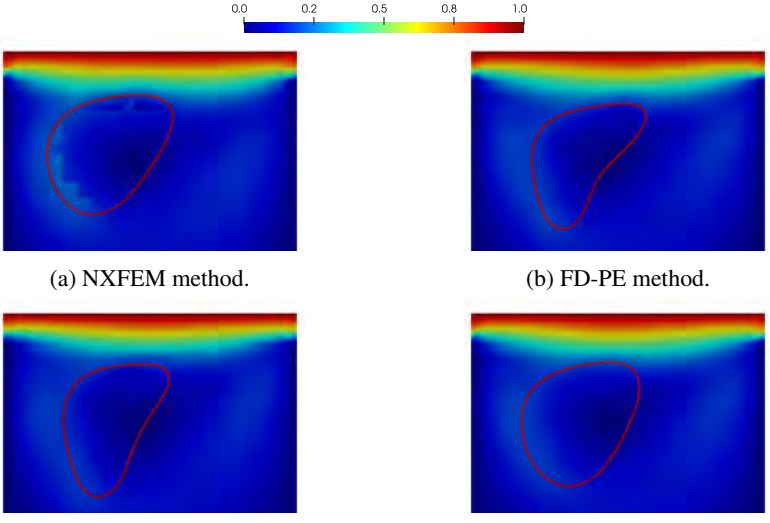

(a) NXFEM method. (b) FD-PE method.

(c) FD-GD method. (d) Algorithm 1.

Figure 27: Snapshots of the fluid velocity magnitude at $t = 4.5$ for the *M1* refinement level.

On the contrary, the FD-GD method yields satisfactory results from the refinement level *M2*, as shown in Figures 28c and 32c.

In this example, fluid incompressibility enforces that the vesicle area remains constant over time. Figure 33 reports the evolution of the vesicle area for the different methods and grid refinement levels. The FD-GD provides reasonable results after grid refinement, Conversely, the FD-PE method exhibits substantial vesicle area variation throughout the simulation at all grid levels, which is clear indication of significant mass losses across the interface. As expected, minimal area changes are observed with Algorithm 1 and the NXFEM method, as the discrete discontinuous pressure prevents interfacial mass loss.

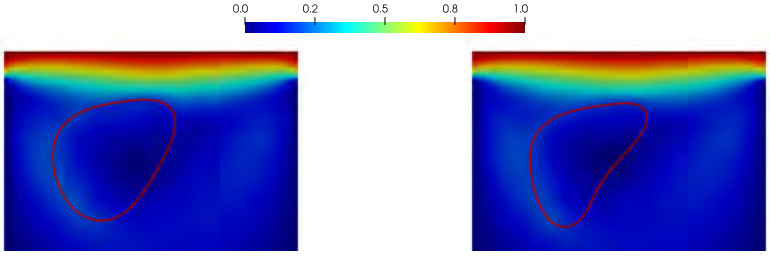

(a) NXFEM method. (b) FD-PE method.

(c) FD-GD method. (d) Algorithm 1.

Figure 28: Snapshots of the fluid velocity magnitude at $t = 4.5$ for the *M2* refinement level.

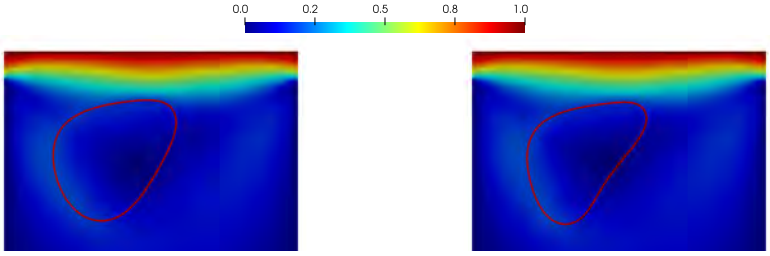

(a) NXFEM method. (b) FD-PE method.

(c) FD-GD method. (d) Algorithm 1.

Figure 29: Snapshots of the fluid velocity magnitude at $t = 4.5$ for the *M3* refinement level.

Figure 34 displays the trajectories of the vesicle point $(0.8, 0.5)$ obtained with the different numerical methods. Since the ALE method cannot be used as a reference, due to the breakdown of the moving-mesh procedure under large interface deformations, the NXFEM solution at finest refinement level, *M3*, is taken as reference. The trajectories provided by NXFEM methods and Algorithm 1 converge after grid refinement. This is much les pronounced for the FD-GD and FD-PE methods. Similar results can be inferred from Table 6, which reports the relative displacement errors. The results show that Algorithm 1 achieves the lowest errors among the FD approaches across all refinement levels. The performance gap becomes increasingly pronounced with mesh refinement, with Algorithm 1 exhibiting approximately two to five times lower errors than the FD-GD and FD-PE approaches at the finest mesh level.

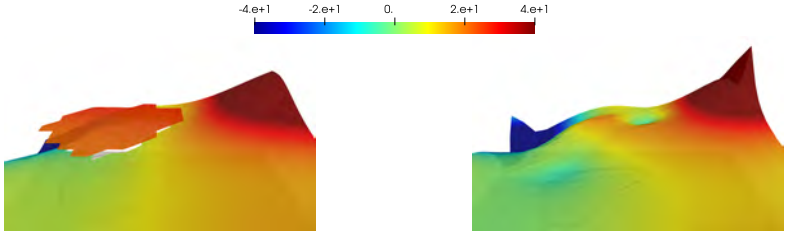

(a) NXFEM method. (b) FD-PE method

(c) FD-GD method. (d) Algorithm 1.

Figure 30: Snapshots of the fluid pressure at $t = 4.5$ for the *M1* refinement level.

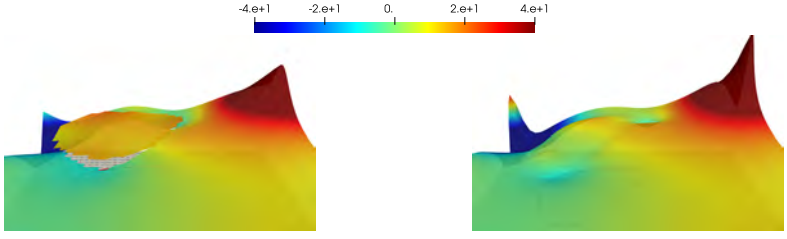

(a) NXFEM method. (b) FD-PE method.

(c) FD-GD method. (d) Algorithm 1.

Figure 31: Snapshots of the fluid pressure at $t = 4.5$ for the *M2* refinement level.

	FD-PE	FD-GD	Algorithm 1
M1	$1.06 \cdot 10^{-1}$	$2.21 \cdot 10^{-1}$	$5.28 \cdot 10^{-2}$
M2	$6.83 \cdot 10^{-2}$	$2.42 \cdot 10^{-1}$	$3.10 \cdot 10^{-2}$
M3	$4.19 \cdot 10^{-2}$	$9.09 \cdot 10^{-2}$	$1.89 \cdot 10^{-2}$

Table 6
Relative L^2 displacement errors of the solid node initially located at $(0.8, 0.5)$ for the different FD methods.

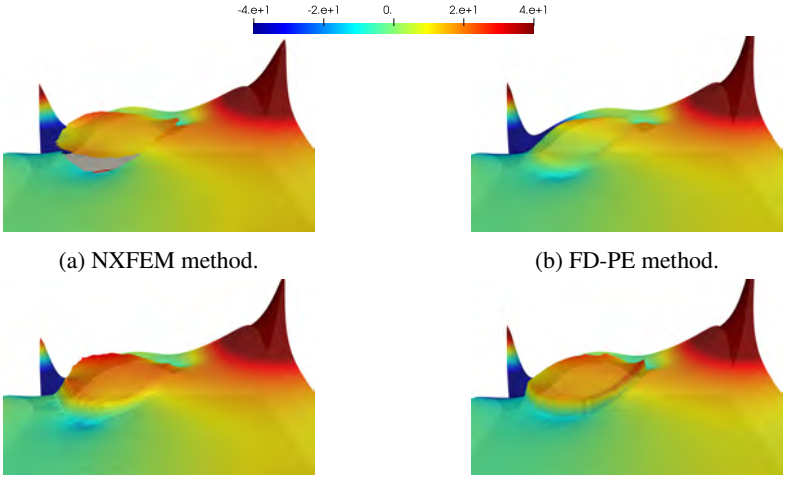

(a) NXFEM method. (b) FD-PE method.

(c) FD-GD method. (d) Algorithm 1.

Figure 32: Snapshots of the fluid pressure at $t = 4.5$ for the *M3* refinement level.

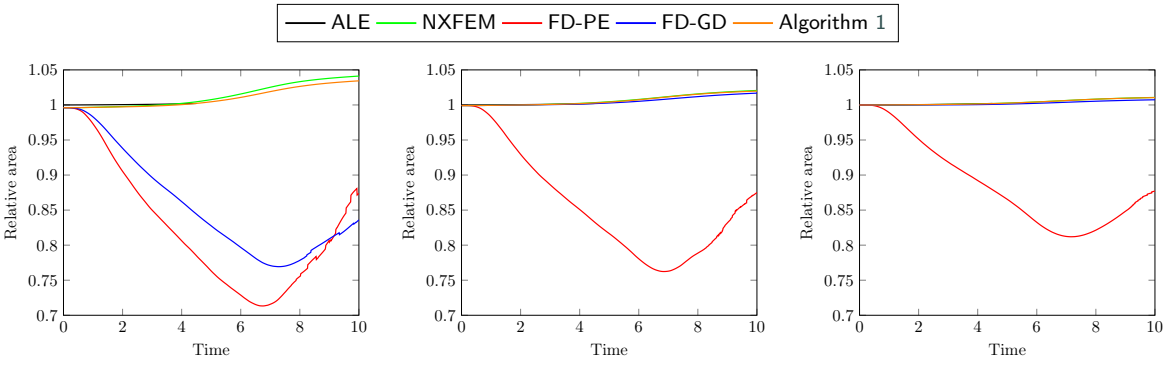

(a) *M1* vs. Reference. (b) *M2* vs. Reference. (c) *M3* vs. Reference.

Figure 33: Time history of the relative area of the vesicle.

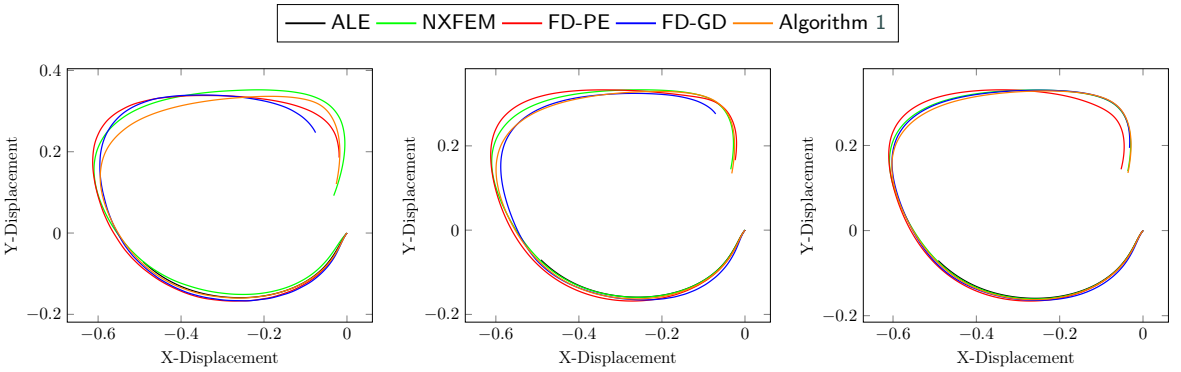

(a) *M1* vs. Reference. (b) *M2* vs. Reference. (c) *M3* vs. Reference.

Figure 34: Trajectory of the interface node initially located at $(0.8, 0.5)$.

4.2. Idealized 3D open valve

In this section, we compare the results provided by Algorithm 1 with the 2D- and 3D-shell models in the 3D counterpart of the example reported in Section 4.1.2. All numerical simulations in this section are carried out using the `FELiScE` finite element library[2] for the fluid subproblem and the 2D-shell subproblem (4), alongside the `MoReFEM` finite element library[3] for the 3D-shell subproblem (6).

Geometrical setting. The fluid domain is defined as $\Omega = (0, 8)\times(0, 0.805)\times(0, 0.5)$, while the reference configuration of the shell is $\Omega^s = (1.9894, 2.0106) \times (0, 0.7) \times (0, 0.5)$, with the mid-surface $\Sigma = \{2\} \times (0, 0.7) \times (0, 0.5)$ (see Figure 35). The simulation is conducted over the time interval $[0, 3]$, which corresponds to three full oscillation cycles of the structure. Boundary conditions include a no-slip condition enforced on Γ_{wall}, a symmetry condition

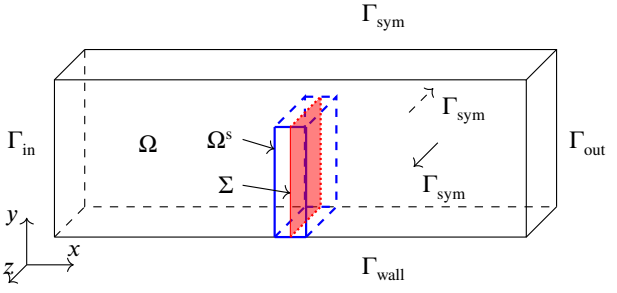

Figure 35: 3D idealized open valve geometric configuration.

on Γ_{sym} (bottom and lateral walls), zero traction on Γ_{out}, and a prescribed parabolic profile on Γ_{in}, given by: $\boldsymbol{u}(t) = -5y(1.61 - y)\,\text{atanh}(5t)(\sin(2\pi t) + 1.1)\boldsymbol{n}$. The structure is clamped at its bottom with symmetry conditions prescribed on its lateral boundaries. Initially, both the fluid and structure are at rest. As in Section 4.1.2, the physical parameters for the fluid in this test are: $\rho^f = 100$ and $\mu = 10$. For the structure, the parameters are: $\rho^s = 100$, $\epsilon = 0.0212$, $E = 5.6 \cdot 10^7$ and $\nu = 0.4$.

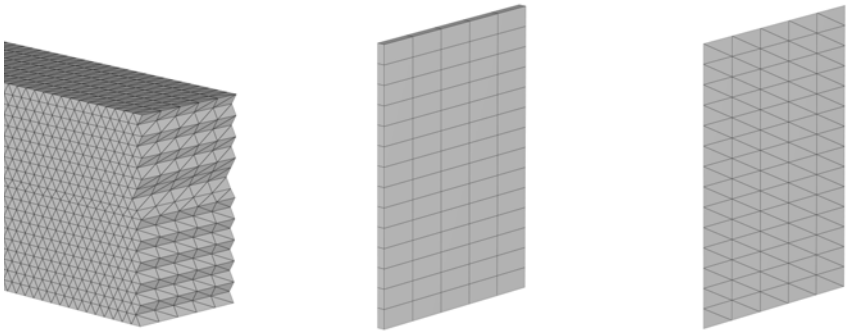

(a) Fluid mesh $\mathcal{T}_h^{\Omega}$.

(b) Solid mesh $\mathcal{T}_{\mathcal{H}}^{\Omega^s}$.

(c) Solid mid-surface triangular mesh $\mathcal{T}_{\mathcal{H}}^{\Sigma}$.

Figure 36: Computational fluid and solid meshes of the 3D open valve example.

Spatial and temporal discretization. The domain Ω is represented by an unstructured simplicial mesh comprising 102150 elements, while the domain Ω^s is defined using a structured grid composed of 70 tensorial shell elements.

[2] `https://gitlab.inria.fr/felisce/felisce`
[3] `https://gitlab.inria.fr/MoReFEM`

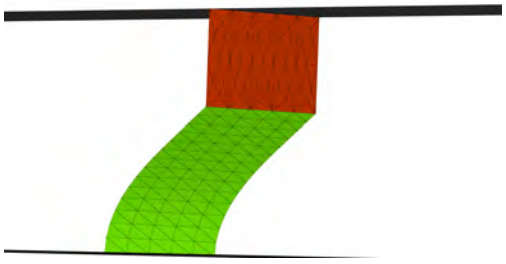

Figure 37: Representation of the solid mid-surface Σ^{n-1} in green and the fictitious interface $\Sigma^{n-1}_{\text{fic}}$ in red.

As a result, the mid-surface Σ is discretized with 140 triangular elements. Both the fluid and structure meshes are characterized by a spatial discretization parameter, h and $\mathcal{H}$ respectively, approximately equal to 0.11. The time-step used is $\tau = 1 \times 10^{-3}$. Additionally, the stabilization parameters are chosen as $\gamma_{\text{SP}} = 1$ and $\gamma_{\text{d}} = 0$ in (24), and $\gamma_{\lambda} = 10$ in (25). At every time step n, the subdomains Ω^n_1 and Ω^n_2 are identified to define the approximation space Q^n using a fictitious interface $\Sigma^{n-1}_{\text{fic}}$. This interface is derived by projecting, at each time step, the immersed upper boundary of Σ^{n-1} onto the boundary Γ_{top}, as depicted in Figure 37. This interface is an extrusion in the z-axis direction of the interface $\Sigma^{n-1}_{\text{fic}}$ illustrated in Figure 15.

Comparison of the results. As in the 2D case of Section 4.1.2., the time-varying velocity profile induces a periodic deflection of the solid. Due to symmetry, the solution is invariant in the z-direction. Figure 38 shows the velocity fields at $t = 0.5$ obtained with Algorithm 1 for the two shell formulations. Overall, the two solutions are in good agreement. Figure 39 provides a comparison of the displacement evolution at the mid-point of the upper leaflet edge. The time

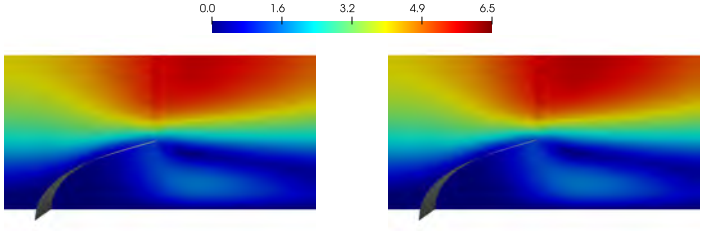

(a) 2D-shell model. (b) 3D-shell model.

Figure 38: Snapshots of the fluid velocity magnitude at $t = 0.5$.

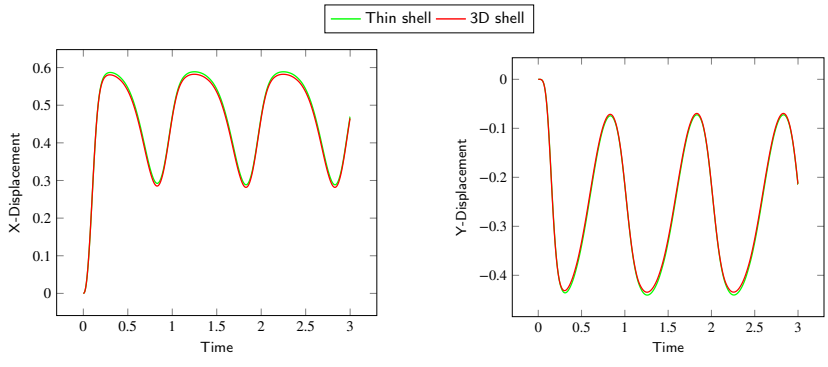

(a) x-displacement. (b) y-displacement.

Figure 39: Time history of the x-displacement (left) and y-displacement (right) of the mid-point of the valve end-edge.

histories indicate a good alignment between the two shell formulations, with a slight divergence near the maximum bending of the structure. Overall, Figure 39 shows that both formulations yield very similar displacement evolutions for this test case.

4.3. Aortic valve with contact

In this section, we investigate the capabilities of Algorithm 1 to simulate the dynamics of the aortic valve over a complete cardiac cycle. In particular, we assess the impact of enhanced mass conservation by comparing the results obtained with Algorithm 1 and those obtained removing the additional mass conservation constraint from it, i.e., by removing the terms involving η^n and χ in Algorithm 1. Hereafter, we refer to this methods as the FD-LG method. Simulating the FSI of the aortic valve presents several challenges. One notable difficulty arises from the large deformations and fast dynamics of the valve during opening and closing phases. Specifically during the closing phase, contact modeling is crucial to prevent leaflet interpenetration. Additionally, when the valve is closed, it experiences substantial pressure gradients, underscoring the importance of preventing mass leakage to ensure the reliability and accuracy of the results.

The numerical simulations in this section were conducted using the `FELiScE` finite element library[4] for the fluid subproblem (28) and the `MoReFEM` finite element library[5] for the solid subproblem (29).

General setting. The aortic root, located between the outflow tract of the left ventricle and the ascending aorta, contains the aortic valve. Specifically, it extends from the superior sinotubular junction to the inferior bases of the valve leaflets. Notably, the aortic root features three sinuses, expanses defined proximally by the attachments of the valve leaflets and distally by the sinotubular junction. In modeling this anatomical region, we consider the domain Ω as a circular rigid tube with a diameter and length of approximately 2 cm, which incorporates the three-lobed dilation of the sinuses near the valve (see Figure 40a). The geometry of the aortic valve with its three leaflets (although, in

(a) Fluid mesh $\mathcal{T}_h^{\Omega}$. (b) Solid mesh $\mathcal{T}_{\mathcal{H}}^{\Omega^s}$. (c) Solid mid-surface triangular mesh $\mathcal{T}_{\mathcal{H}}^{\Sigma}$.

Figure 40: Computational meshes of the aortic valve.

pathological cases, they may reduce to two) is represented in Figure 40c. The thickness of the leaflets is approximately $\epsilon = 3.86 \cdot 10^{-2}$ cm. Valve mechanics, including leaflet contact, are described by the 3D-shell model of Section 2.1.2.

We define the inflow and outflow boundaries as the bottom and top boundaries of Ω lying on the ventricular and aortic sides, respectively (see Figure 40a). At the inflow boundary, denoted as Γ_{in}, we prescribe the idealized left ventricular pressure profile illustrated in Figure 41 and adapted from [47]. The temporal domain is defined as $t \in [0, 0.342]$, corresponding to a single cardiac cycle (opening and closure). Conversely, at the outflow boundary, denoted as Γ_{out}, we apply the resistance boundary condition $\boldsymbol{\sigma}^{\text{f}}(\boldsymbol{u}, p)\boldsymbol{n} = -(p_0 + RQ)\boldsymbol{n}$, where $p_0 = 80$ mmHg represents a constant physiological pressure level, Q denotes the volumetric flow rate through the outflow (with the convention that $Q > 0$ indicates flow leaving the domain), $R = 70\,(\text{dyn} \cdot \text{s})/\text{cm}^5$ is a resistance constant (see [47]).

These parameters ensure a realistic transvalvular pressure difference of 80 mmHg during the diastolic steady state (where Q is nearly zero), while permitting a reasonable flow rate during systole. On the wall of the aortic root, denoted by Γ_w, we impose the no-slip boundary condition $\boldsymbol{u} = \boldsymbol{0}$. Backflow stabilization is applied both on Γ_{in} and Γ_{out} to avoid the traditional instability issues of the Navier-Stokes approximations with Neumann boundary conditions (see,

[4] `https://gitlab.inria.fr/felisce/felisce`
[5] `https://gitlab.inria.fr/MoReFEM`

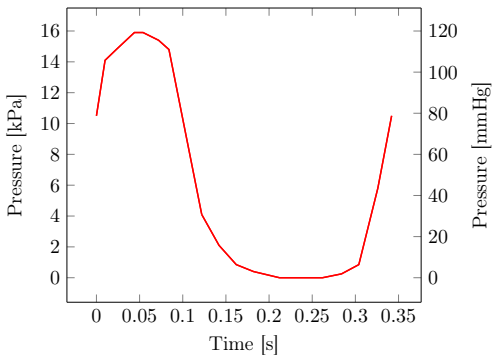

Figure 41: Idealized left ventricular (LV) pressure profile applied to the inflow boundary Γ_{in} (see [47])

Algorithm 2 Triangulation of the fictitious interface $\Sigma_{\text{fic}}^{n-1}$, as shown in Figure 42.

Input: $\Sigma_{\text{fic}}^{n-1}$ boundary edges.

1. Add the central triangle ABC to $\mathcal{T}_{\mathcal{H}}^{\Sigma_{\text{fic}}^{n-1}}$.
2. Starting from edge BA, consider vertices R and S to form triangles BAR and BAS. Select the triangle with higher quality, e.g., BAS, and add it to $\mathcal{T}_{\mathcal{H}}^{\Sigma_{\text{fic}}^{n-1}}$.
3. Starting from edge SA, consider vertices R and H to form triangles SAR and SAH. Again, select the triangle with higher quality, e.g., SAR, and add it to $\mathcal{T}_{\mathcal{H}}^{\Sigma_{\text{fic}}^{n-1}}$.
4. Repeat step (3) for edge SR to obtain SRC, for edge SC to obtain SCH, etc.
5. From edge QP, the only available vertex is D. Add the triangle to $\mathcal{T}_{\mathcal{H}}^{\Sigma_{\text{fic}}^{n-1}}$.
6. Finally, the obtained triangulation is appropriately refined.

Output: Triangulation $\mathcal{T}_{\mathcal{H}}^{\Sigma_{\text{fic}}^{n-1}}$.

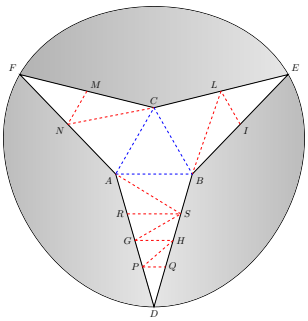

Figure 42: Schematic representation of the construction of the fictitious interface $\Sigma_{\text{fic}}^{n-1}$. Top view of the aortic valve. In *gray* the valve leaflets.

e.g., [9]). At time $t = 0$, the system is at rest; notably, the inflow pressure condition on Γ_{in} of Figure 41 coincides with p_0.

The fluid parameters, which reflect the physical properties of human blood (see, e.g., [48, 65]), are defined as $\rho^{\mathrm{f}} = 1.0\,\mathrm{g/cm^3}$ and $\mu = 3 \cdot 10^{-2}\,\mathrm{g/(cm \cdot s)}$. For the valve leaflets, we adopt an isotropic St. Venant–Kirchhoff material model with $E = 1 \cdot 10^7 \mathrm{dyn/cm^2}$ and $\nu = 0.499$. The solid density is $\rho^{\mathrm{s}} = 1.2\,\mathrm{g/cm^3}$.

Spatial and temporal discretization. The fluid domain Ω is discretized using a simplicial mesh composed of 607 046 tetrahedral elements, each with a characteristic size of approximately $h \approx 0.045\,\mathrm{cm}$ (see Figure 40a). The computational mesh of the bulk solid domain Ω^{s} consists of 17 888 prismatic $\mathbb{Q}_1 \otimes \mathbb{P}_2$ elements (see Figure 40b). The corresponding triangular mesh of its mid-surface Σ, where the FSI coupling and penalty contact terms are evaluated, comprises 35 776 triangles with an approximate characteristic size of $\mathcal{H} \approx 0.035\,\mathrm{cm}$ (see Figure 40c). The time-step length chosen for the simulation is $\tau = 10^{-4}\,\mathrm{s}$. Additionally, we set $\gamma_{\mathrm{SP}} = 1$ in the SUPG/PSPG stabilization (24), and the Lagrange multiplier stabilization parameter to $\gamma_\lambda = 10^3$ in (25).

(a) $t = 0.015$. (b) $t = 0.080$. (c) $t = 0.250$.

Figure 43: Fictitious interface generated by Algorithm 2 at three different time steps.

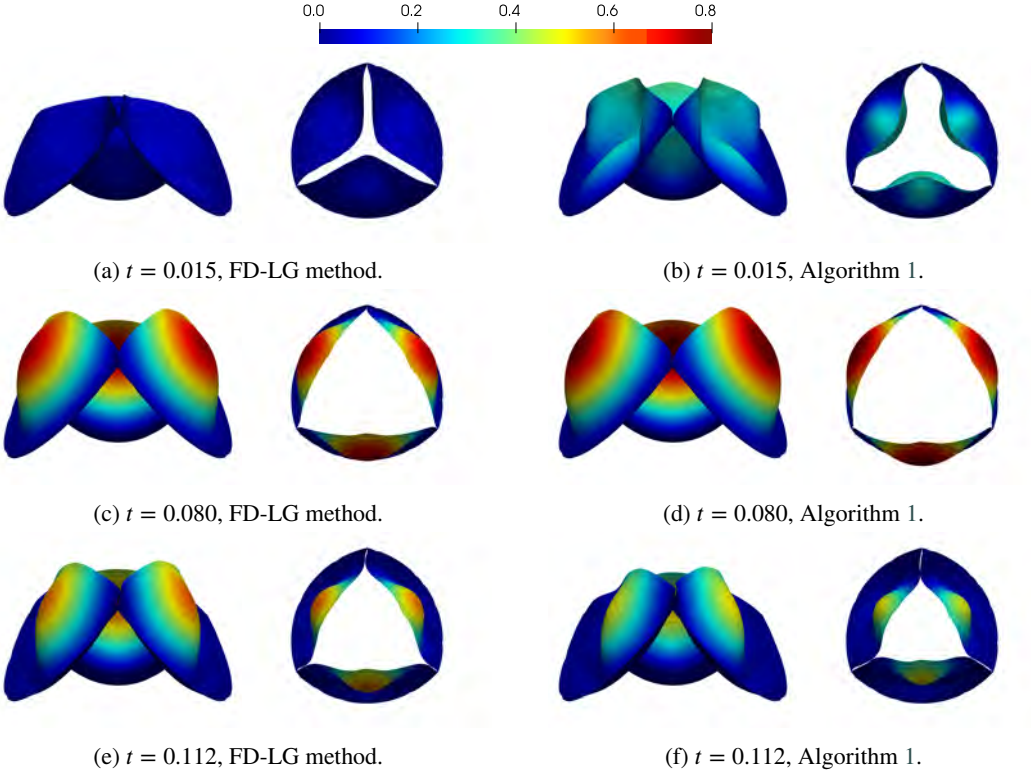

(a) $t = 0.015$, FD-LG method. (b) $t = 0.015$, Algorithm 1.

(c) $t = 0.080$, FD-LG method. (d) $t = 0.080$, Algorithm 1.

(e) $t = 0.112$, FD-LG method. (f) $t = 0.112$, Algorithm 1.

Figure 44: Snapshots of the valve deformation from two perspectives: top view and side view, colored by displacement magnitude.

To prevent artificial penetration between the valve leaflets, the contact condition (8) is approximated as $\mathrm{dist}\big(\boldsymbol{x}, \Sigma(t)\big) \geq \varepsilon_{\mathrm{g}}$, where $\varepsilon_{\mathrm{g}} > 0$ denotes the so-called contact relaxation tolerance. From an implementation standpoint, this simply amounts to replacing $\mathrm{dist}\big(\boldsymbol{x}, \Sigma(t)\big)$ with $\mathrm{dist}\big(\boldsymbol{x}, \Sigma(t)\big) - \varepsilon_{\mathrm{g}}$ in the penalized contact energy (13). The contact penalty parameter is set to $\kappa_{\mathrm{c}} = 5 \times 10^7$, while the contact relaxation tolerance is set to $\varepsilon_{\mathrm{g}} = 0.02, \mathrm{cm}$, which is approximately $h/2$.

At each time level n, the fictitious interface $\Sigma_{\mathrm{fic}}^{n-1}$ must be constructed to allow the definition of the two fluid subdomains, Ω_1^{n-1} and Ω_2^{n-1}, involved in the definition (20) of the discrete pressure space Q_h^n. A triangulation $\mathcal{T}_{\mathcal{H}}^{\Sigma_{\mathrm{fic}}^{n-1}}$ of $\Sigma_{\mathrm{fic}}^{n-1}$ is constructed following the steps outlined in Algorithm 2 and illustrated in Figure 42. Figure 43 shows the fictitious interface generated by Algorithm 2 at three different time steps. It should be noted that no unknowns are defined on this mesh, which is solely used for integration purposes. Algorithm 2 is implemented within the software `Wolf`[6].

Comparison of the results. The numerical simulation starts almost at the beginning of the systolic phase, precisely at the conclusion of the isovolumetric ventricular contraction.

During this phase, as the ventricular pressure steadily increases, the aortic valve begins to open, allowing blood flow from the left ventricle into the aorta. As the blood is propelled into the aorta, the ventricular pressure gradually decreases until it falls below the aortic pressure, resulting in a slight backward flow. This backward flow prompts the closure of the aortic valve, vanishing with it. Subsequently, the diastolic phase begins, with the left ventricle and the aorta separated by the closed aortic valve, and only minimal blood recirculation on both sides of the valve is experienced. The ventricular pressure then resumes increasing, marking the beginning of a new cardiac cycle.

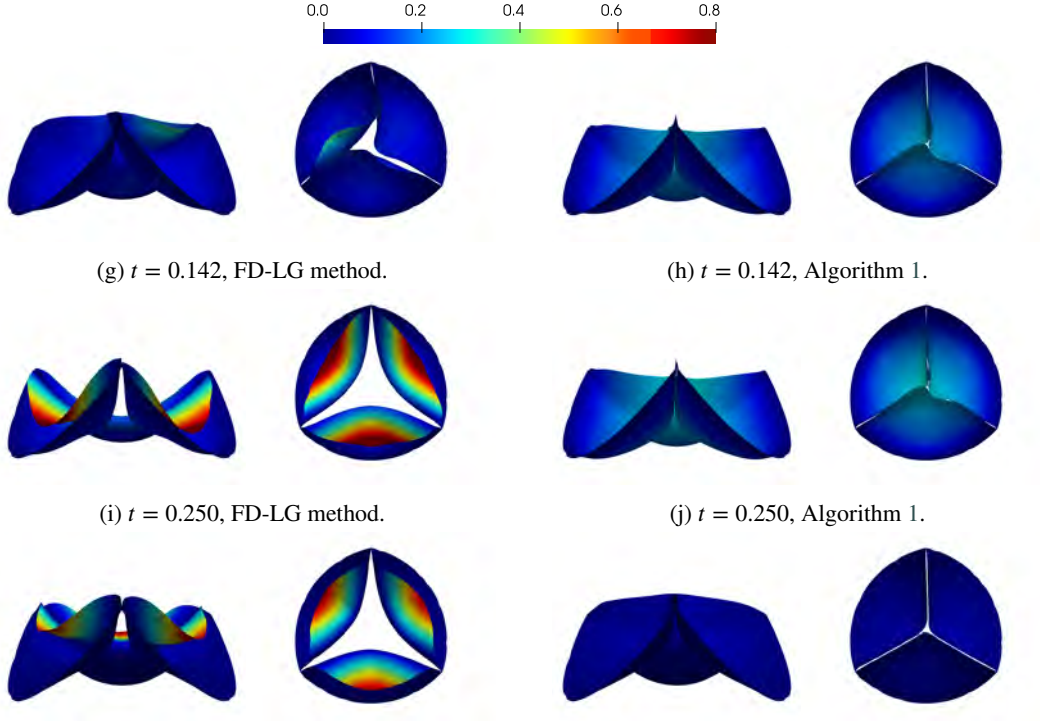

(g) $t = 0.142$, FD-LG method. (h) $t = 0.142$, Algorithm 1.

(i) $t = 0.250$, FD-LG method. (j) $t = 0.250$, Algorithm 1.

(k) $t = 0.342$, FD-LG method. (l) $t = 0.342$, Algorithm 1.

Figure 44: Snapshots of the valve deformation from two perspectives: top view and side view, colored by displacement magnitude.

Figures 45 and 44 provide some snapshots of the fluid velocity field and mid-surface valve deformation, respectively, for both Algorithm 1 and the FD-LG approach. Algorithm 1 clearly provides superior interfacial mass

[6] https://team.inria.fr/gamma/gamma-software/

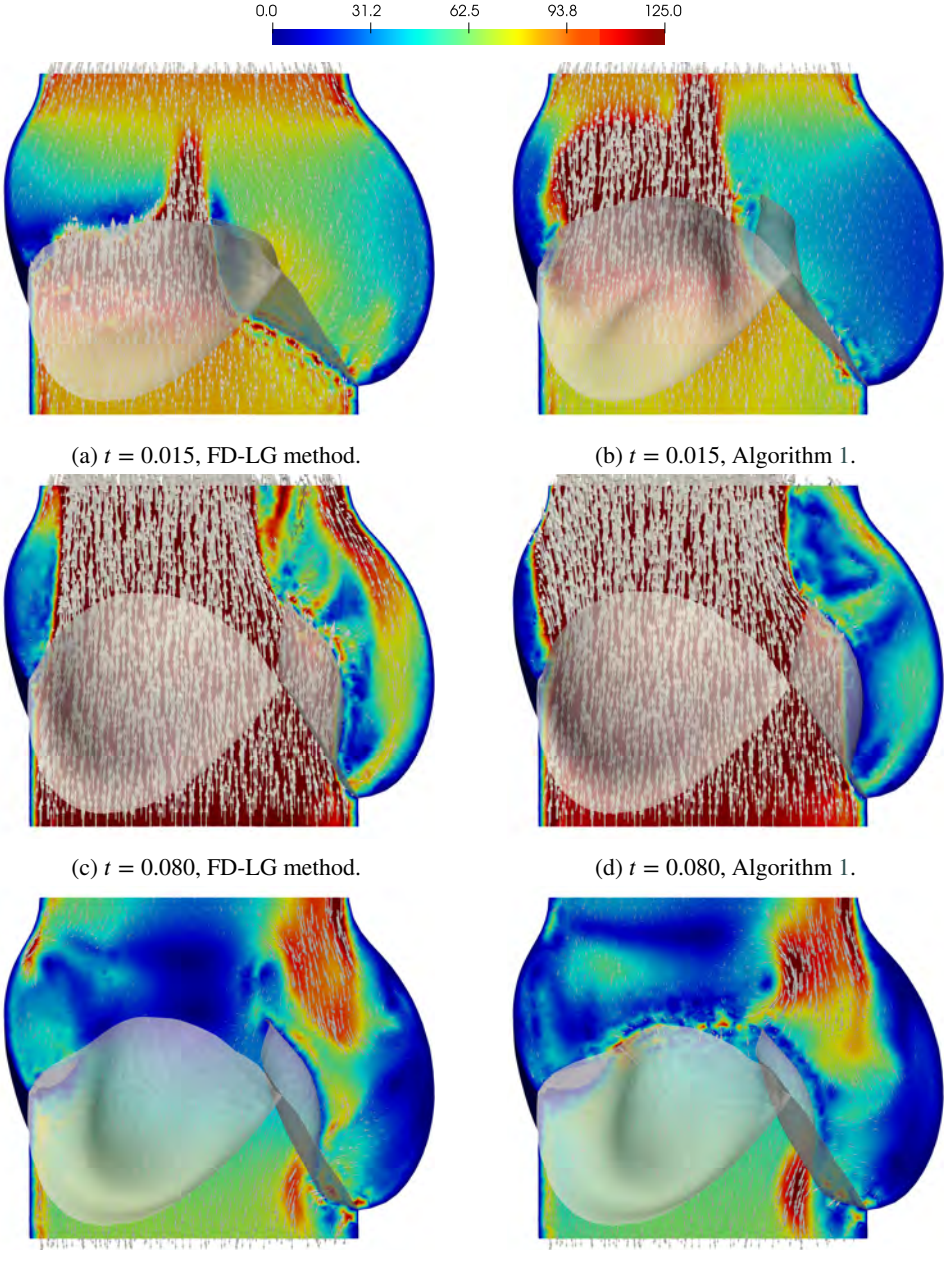

(a) $t = 0.015$, FD-LG method.

(b) $t = 0.015$, Algorithm 1.

(c) $t = 0.080$, FD-LG method.

(d) $t = 0.080$, Algorithm 1.

(e) $t = 0.112$, FD-LG method.

(f) $t = 0.112$, Algorithm 1.

Figure 45: Snapshots of the fluid velocity field at multiple time steps throughout a cardiac cycle. Left: Results obtained using the FD-LG method. Right: Results obtained using Algorithm 1.

conservation with respect to the FD-LG method. In particular, significant spurious velocity and a lack of mass conservation are observed across the valve leaflets with the FD-LG method during the initial stages of valve opening ($t = 0.015$), in contrast to the behavior exhibited by Algorithm 1 (see Figures 45a-b). As a result, the fluid-induced stress on the valve leaflets is lower with the FD-LG method compared to Algorithm 1, leading to reduced leaflet displacement (see Figures 44a-b). The discrepancy in valve displacement between the two methods is evident throughout the entire simulation, with a more pronounced contrast observed during the transition between the open and closed configurations (refer to Figures 44a-b-e-f). Even at maximum valve opening, this difference persists, with the valve position slightly more closed in the FD-LG method compared to Algorithm 1 (see Figures 44c-d).

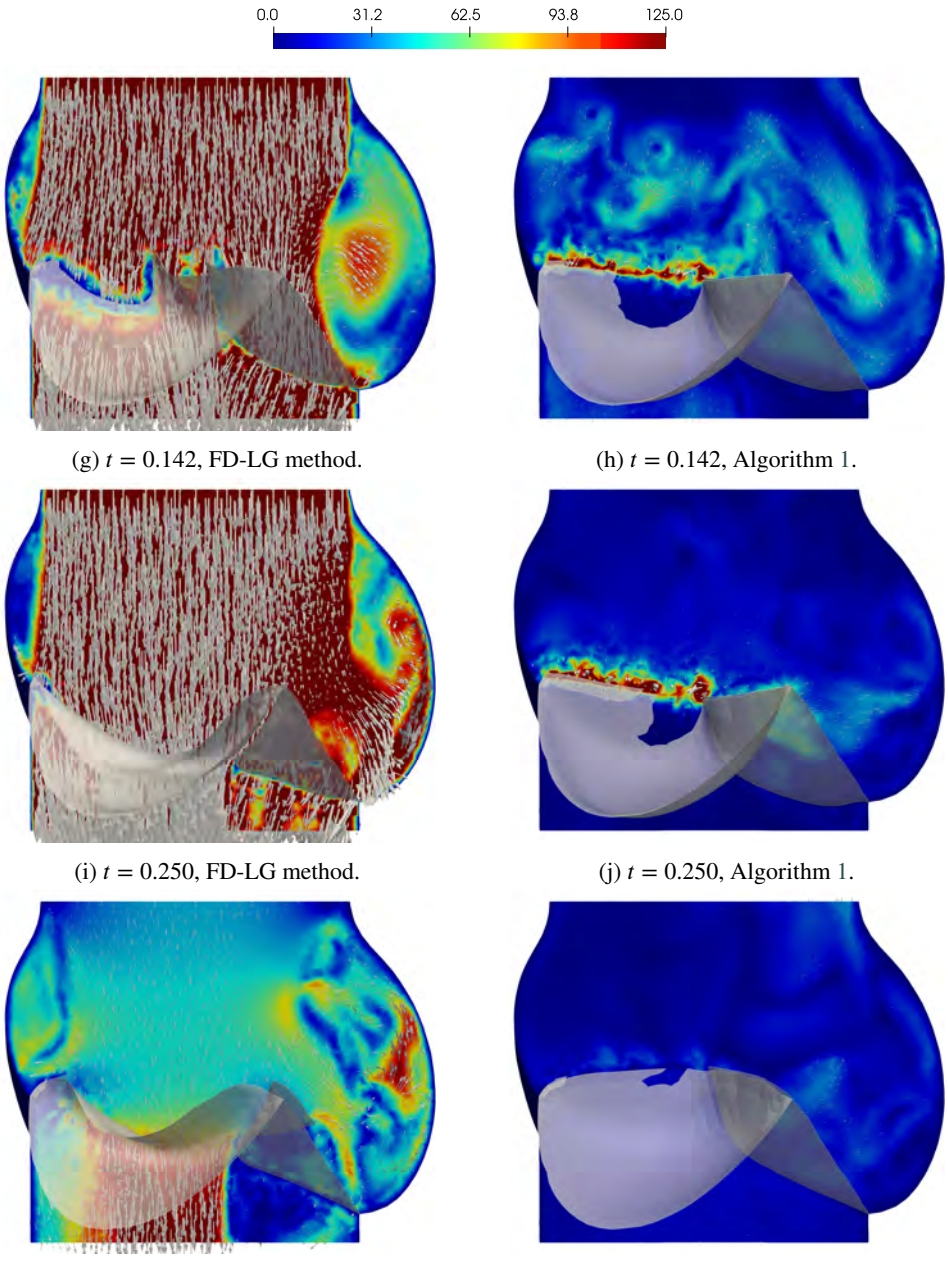

(g) $t = 0.142$, FD-LG method.

(h) $t = 0.142$, Algorithm 1.

(i) $t = 0.250$, FD-LG method.

(j) $t = 0.250$, Algorithm 1.

(k) $t = 0.342$, FD-LG method.

(l) $t = 0.342$, Algorithm 1.

Figure 45: Snapshots of the fluid velocity field at multiple time steps throughout a cardiac cycle. Left: Results obtained using the FD-LG method. Right: Results obtained using Algorithm 1.

At this point, Figures 45c-d show a significant blood flow from the left ventricle into the aorta, i.e., from Γ_{in} to Γ_{out}. Although Algorithm 1 demonstrates enhanced mass conservation compared to the FD-LG method, both methodologies reveal some degree of mass leakage near the valve attachment to the aortic root wall. Notably, this leakage is less pronounced when utilizing Algorithm 1. The emergence of this spurious velocity is attributed to the relatively coarse resolution and is expected to diminish with increased levels of refinement.

During the closure phase, a flow is observed from Γ_{out} to Γ_{in} owing to the higher pressure in the aorta compared to the ventricle (see Figures 45e-f). As the valve gradually closes, the enhanced mass conservation offered by Algorithm 1 becomes more prominent. Under these circumstances, the velocity field is expected to gradually decrease, eventually

showing only minimal recirculation phenomena on each side of the valve when the valve is fully closed. However, with the FD-LG method, significant velocity fields persist, resulting in substantial mass leakage (see Figures 45g-i), whereas Algorithm 1 demonstrates a gradual reduction of blood recirculation after an initial transition period (see Figures 45h-j). In particular, the presence of spurious velocity in the FD-LG leads to a non-natural twisting motion (see Figure 44g), which causes partial detachment of the leaflets and the formation of spaces that allow induced blood flow across the valve. Over time, this continuous flow causes the leaflets to fold back on themselves (see Figure 44i), creating an even larger opening that permits substantial blood leakage (see Figure 45i), while in contrast, the Algorithm 1 maintains proper valve closure with minimal flow disturbances (see Figures 44j and 45j).

Figures 45h-j show minor fluid leakage along the contact region between the valve leaflets. This leakage is ascribed to the contact relaxation parameter ε_g employed in the contact algorithm to avoid penetration. Nonetheless, decreasing the value of the contact relaxation parameter ε_g is expected to mitigate this phenomenon. Figures 45k-l, captured at the initial stage of the valve opening phase, exhibit similar trends to those observed at previous time instances for both methods.

5. Conclusion

We have proposed a fictitious domain method for immersed FSI with enhanced mass conservation based on the symmetric variant of the method presented in [27]. The behavior of the immersed thin-walled structure was modeled using both 2D and 3D-shell models. A salient feature of the proposed method is that the size of the system matrix remains constant regardless of the location of the interface with respect to the background computational mesh, which is particularly advantageous for cases involving moving interfaces. This innovative fictitious domain method for immersed fluid-structure interaction has been compared and validated through a series of 2D benchmarks, encompassing fully non-linear models and large interface deflections, alongside alternative numerical approaches. The proposed approach demonstrates similar or superior accuracy compared to alternative fictitious domain methods. Notably, it achieves this without the necessity of resorting to penalty terms, which can compromise the conditioning of the resulting system matrix. Furthermore, the accuracy achieved is comparable to that of the Nitsche-XFEM method, provided a reasonable level of mesh refinement is used. In the numerical test under consideration, both shell models produce comparable results; however, the 3D-shell formulation offers distinct advantages. Notably, it facilitates coupling with other 3D media, e.g., the aortic valve with the left ventricle, enables the use of arbitrary 3D material laws, and provides more precise information throughout the body's thickness. Finally, the method has been successfully applied to the simulation of the aortic valve under realistic conditions. The improvement in mass conservation ensured by the proposed method is notably evident when the valve is closed, in contrast to the standard fictitious domain method, leading to an overall satisfactory solution.

Funding

This work was funded by the French National Research Agency (ANR), through the SIMR project (ANR-19-CE45-0020).

Declaration of competing interest

The authors declare that there are no known conflicts of interest associated with this work.

Data availability

Data will be made available on request.

Acknowledgement

The authors wish to thank Frédéric Alauzet (Inria) for the inspiring discussions on the triangulation of the fictitious interface.

References

[1] F. Alauzet. A changing-topology moving mesh technique for large displacements. *Engineering with Computers*, 30(2):175–200, 2014.

[2] F. Alauzet, B. Fabrèges, M. A. Fernández, and M. Landajuela. Nitsche-XFEM for the coupling of an incompressible fluid with immersed thin-walled structures. *Computer Methods in Applied Mechanics and Engineering*, 301:300–335, 2016.
[3] M. Astorino, J.-F. Gerbeau, O. Pantz, and K.-F. Traore. Fluid–structure interaction and multi-body contact: application to aortic valves. *Computer Methods in Applied Mechanics and Engineering*, 198(45-46):3603–3612, 2009.
[4] F. P. T. Baaijens. A fictitious domain/mortar element method for fluid–structure interaction. *International Journal for Numerical Methods in Fluids*, 35(7):743–761, 2001.
[5] Y. Bao, A. Donev, B.E. Griffith, D.M. McQueen, and C.S. Peskin. An immersed boundary method with divergence-free velocity interpolation and force spreading. *Journal of Computational Physics*, 347:183–206, 2017.
[6] G. R. Barrenechea and C. González. A stabilized finite element method for a fictitious domain problem allowing small inclusions. *Numerical Methods for Partial Differential Equations*, 34(1):167–183, 2018.
[7] K. J. Bathe. *Finite Element Procedures*. Prentice Hall, 1996.
[8] M. Bergmann, A. Fondanèche, and A. Iollo. An Eulerian finite-volume approach of fluid-structure interaction problems on quadtree meshes. *Journal of Computational Physics*, 471:111647, 2022.
[9] C. Bertoglio, A. Caiazzo, Y. Bazilevs, M. Braack, M. Esmaily, V. Gravemeier, A. L. Marsden, O. Pironneau, I. E. Vignon-Clementel, and W. A. Wall. Benchmark problems for numerical treatment of backflow at open boundaries. *International Journal for Numerical Methods in Biomedical Engineering*, 34(2):e2918, 2018.
[10] M. Bischoff, K. U. Bletzinger, W. A. Wall, and E. Ramm. Models and finite elements for thin-walled structures. In *Encyclopedia of Computational Mechanics*, chapter 2. John Wiley & Sons, 2004.
[11] D. Boffi and L. Gastaldi. A fictitious domain approach with Lagrange multiplier for fluid-structure interactions. *Numerische Mathematik*, 135 (3):711–732, 2017.
[12] D. Boffi, N. Cavallini, and L. Gastaldi. Finite element approach to immersed boundary method with different fluid and solid densities. *Mathematical Models and Methods in Applied Sciences*, 21(12):2523–2550, 2011.
[13] D. Boffi, N. Cavallini, F. Gardini, and L. Gastaldi. Stabilized Stokes elements and local mass conservation. *Bollettino dell'Unione Matematica Italiana*, 5(3):543–573, 2012.
[14] D. Boffi, N. Cavallini, F. Gardini, and L. Gastaldi. Local mass conservation of Stokes finite elements. *Journal of Scientific Computing*, 52: 383–400, 2012.
[15] D. Boffi, N. Cavallini, and L. Gastaldi. The finite element immersed boundary method with distributed Lagrange multiplier. *SIAM Journal on Numerical Analysis*, 53(6):2584–2604, 2015.
[16] L. Boilevin-Kayl, M. A. Fernández, and J.-F. Gerbeau. Numerical methods for immersed FSI with thin-walled structures. *Computers & Fluids*, 179:744–763, 2019.
[17] E. Burman and M. A. Fernández. An unfitted Nitsche method for incompressible fluid–structure interaction using overlapping meshes. *Computer Methods in Applied Mechanics and Engineering*, 279:497–514, 2014.
[18] E. Burman and P. Hansbo. Fictitious domain methods using cut elements: III. A stabilized Nitsche method for Stokes' problem. *ESAIM: Mathematical Modelling and Numerical Analysis*, 48:497–514, 2014.
[19] E. Burman, P. Hansbo, and M. G. Larson. Cut finite element method for divergence free approximation of incompressible flow: optimal error estimates and pressure independence, 2022.
[20] H. Casquero, C. Bona-Casas, and H. Gomez. NURBS-based numerical proxies for red blood cells and circulating tumor cells in microscale blood flow. *Computer Methods in Applied Mechanics and Engineering*, 316:646–667, 2017.
[21] H. Casquero, C. Bona-Casas, D. Toshniwal, T.J.R. Hughes, H. Gomez, and Y. Jessica Zhang. The divergence-conforming immersed boundary method: Application to vesicle and capsule dynamics. *Journal of Computational Physics*, 425:109872, 2021.
[22] D. Chapelle and K. J. Bathe. *The finite element analysis of shells - Fundamentals*. Springer Science & Business Media, 2010.
[23] D. Chapelle and A. Ferent. Modeling of the inclusion of a reinforcing sheet within a 3D medium. *Mathematical Models and Methods in Applied Sciences*, 13(04):573–595, 2003.
[24] D. Chapelle and I. Paris. Detailed reliability assessment of triangular MITC elements for thin shells. *Computers & Structures*, 86(23): 2192–2202, 2008.
[25] D. Chapelle, A. Ferent, and K. J. Bathe. 3D-shell elements and their underlying mathematical model. *Mathematical Models and Methods in Applied Sciences*, 14(1):105–142, 2004.
[26] S. H. Christiansen and K. Hu. Generalized finite element systems for smooth differential forms and Stokes'problem. *Numerische Mathematik*, 140(2):327–371, 2018.
[27] D. C. Corti, G. Delay, M. A. Fernández, F. Vergnet, and M. Vidrascu. Low-order fictitious domain method with enhanced mass conservation for an interface stokes problem. *ESAIM: Mathematical Modelling and Numerical Analysis*, 58(1):303–333, 2024.
[28] J. De Hart, G.W.M. Peters, P.J.G. Schreurs, and F.P.T. Baaijens. A three-dimensional computational analysis of fluid–structure interaction in the aortic valve. *Journal of Biomechanics*, 36(1):103–112, 2003.
[29] S. Deparis, M. Discacciati, G. Fourestey, and A. Quarteroni. Fluid-structure algorithms based on Steklov-Poincaré operators. *Computer Methods in Applied Mechanics and Engineering*, 195(41-43):5797–5812, 2006.
[30] J. Donea, S. Giuliani, and J.-P. Halleux. An arbitrary Lagrangian-Eulerian finite element method for transient dynamic fluid-structure interactions. *Computer Methods in Applied Mechanics and Engineering*, 33(1-3):689–723, 1982.
[31] N. D. Dos Santos, J.-F. Gerbeau, and J.-F. Bourgat. A partitioned fluid–structure algorithm for elastic thin valves with contact. *Computer Methods in Applied Mechanics and Engineering*, 197(19):1750–1761, 2008.
[32] M. A. Fernández and M. Moubachir. A Newton method using exact Jacobians for solving fluid-structure coupling. *Computers & Structures*, 83(2-3):127–142, 2005.
[33] L. Formaggia and F. Nobile. A stability analysis for the arbitrary Lagrangian Eulerian formulation with finite elements. *East-West Journal of Numerical Mathematics*, 7(2):105–131, 1999.

[34] K. J. Galvin, A. Linke, L. G. Rebholz, and N. E. Wilson. Stabilizing poor mass conservation in incompressible flow problems with large irrotational forcing and application to thermal convection. *Computer Methods in Applied Mechanics and Engineering*, 237/240:166–176, 2012.
[35] M. A. George, N. Williamson, and S. W. Armfield. Mass-conserving ghost cell immersed boundary method with multigrid for coupled navier-stokes solvers. *Journal of Computational Physics*, 540:114276, 2025.
[36] A. Gerstenberger and W. A. Wall. An extended finite element method/Lagrange multiplier based approach for fluid–structure interaction. *Computer Methods in Applied Mechanics and Engineering*, 197(19-20):1699–1714, 2008.
[37] A. J. Gil, A. Arranz Carreño, J. Bonet, and O. Hassan. An enhanced Immersed Structural Potential Method for fluid-structure interaction. *Journal of Computational Physics*, 250:178–205, 2013.
[38] B. E. Griffith. Immersed boundary model of aortic heart valve dynamics with physiological driving and loading conditions. *International Journal for Numerical Methods in Biomedical Engineering*, 28(3):317–345, 2012.
[39] B. E. Griffith and X. Luo. Hybrid finite difference/finite element immersed boundary method. *International Journal for Numerical Methods in Biomedical Engineering*, 33(12):e2888, 2017.
[40] S. Groß and A. Reusken. An extended pressure finite element space for two-phase incompressible flows with surface tension. *Journal of Computational Physics*, 224(1):40–58, 2007.
[41] C. Gruninger and B.E. Griffith. Composite B-spline regularized delta functions for the immersed boundary method: Divergence-free interpolation and gradient-preserving force spreading. *Journal of Computational Physics*, 546:114472, 2026. ISSN 0021-9991.
[42] E. Hachem, S. Feghali, R. Codina, and T. Coupez. Immersed stress method for fluid-structure interaction using anisotropic mesh adaptation. *International Journal for Numerical Methods in Engineering*, 94(9):805–825, 2013.
[43] J. Haslinger and Y. Renard. A new fictitious domain approach inspired by the extended finite element method. *SIAM Journal on Numerical Analysis*, 47, 2009.
[44] C. Hesch, A. J. Gil, A. Arranz Carreño, and J. Bonet. On continuum immersed strategies for Fluid-Structure Interaction. *Computer Methods in Applied Mechanics and Engineering*, 247-248:51–64, 2012.
[45] J. Hoffman, J. Jansson, and M. Stöckli. Unified continuum modeling of fluid-structure interaction. *Mathematical Models and Methods in Applied Sciences*, 21(03):491–513, 2011.
[46] J. Jansson, N. C. Degirmenci, and J. Hoffman. Adaptive unified continuum FEM modeling of a 3D FSI benchmark problem. *International journal for numerical methods in biomedical engineering*, 33(9):e2851, 2017.
[47] D. Kamensky, M.-C. Hsu, D. Schillinger, J. A. Evans, A. Aggarwal, Y. Bazilevs, M. S. Sacks, and T. J. R. Hughes. An immersogeometric variational framework for fluid–structure interaction: Application to bioprosthetic heart valves. *Computer Methods in Applied Mechanics and Engineering*, 284:1005–1053, 2015.
[48] T. Kenner. The measurement of blood density and its meaning. *Basic Research in Cardiology*, 84(2):111–124, 1989.
[49] J. Kim, D. Kim, and H. Choi. An immersed-boundary finite-volume method for simulations of flow in complex ceometries. *Journal of Computational Physics*, 171(1):132–150, 2001.
[50] M. Landajuela, M. Vidrascu, D. Chapelle, and M. A. Fernández. Coupling schemes for the FSI forward prediction challenge: comparative study and validation. *International journal for numerical methods in biomedical engineering*, 33(4):e2813, 2017.
[51] J. Lee and D. You. An implicit ghost-cell immersed boundary method for simulations of moving body problems with control of spurious force oscillations. *Journal of Computational Physics*, 233:295–314, 2013.
[52] L. Lee and R.J. LeVeque. An immersed interface method for incompressible Navier–Stokes equations. *SIAM Journal on Scientific Computing*, 25(3):832–856, 2003.
[53] P. S. Lee and K. J. Bathe. Development of MITC isotropic triangular shell finite elements. *Computers & Structures*, 82(11):945–962, 2004.
[54] J. Liu and A. L. Marsden. A unified continuum and variational multiscale formulation for fluids, solids, and fluid–structure interaction. *Computer Methods in Applied Mechanics and Engineering*, 337:549–597, 2018.
[55] Y. Liu and W.K. Liu. Rheology of red blood cell aggregation by computer simulation. *Journal of Computational Physics*, 220(1):139–154, 2006.
[56] R. D. Mindlin. Influence of rotary inertia and shear on flexural motions of isotropic elastic plates. *Journal of Applied Mechanics*, 18:31–38, 1951.
[57] R. Mittal and G. Iaccarino. Immersed boundary methods. *Annual Review of Fluid Mechanics*, 37(1):239–261, 2005.
[58] P. Moireau, D. Chapelle, and P. Le Tallec. Filtering for distributed mechanical systems using position measurements: Perspectives in medical imaging. *Inverse Problems*, 25:35010–25, 2009.
[59] T. Nakata and H. Liu. A fluid–structure interaction model of insect flight with flexible wings. *Journal of Computational Physics*, 231(4): 1822–1847, 2012.
[60] T. Nomura and T.J.R. Hughes. An arbitray Lagrangian-Eulerian finite element method for interaction of fluid and rigid body. *Computer Methods in Applied Mechanics and Engineering*, 95(1):115–138, 1992.
[61] C. S. Peskin. The immersed boundary method. *Acta numerica*, 11:479–517, 2002.
[62] C. S. Peskin and B. F. Printz. Improved volume conservation in the computation of flows with immersed elastic boundaries. *Journal of Computational Physics*, 105(1):33–46, 1993.
[63] K. Poulios and Y. Renard. An unconstrained integral approximation of large sliding frictional contact between deformable solids. *Computers & Structures*, 153:75–90, 2015.
[64] E. Reissner. The effect of transverse shear deformation on the bending of elastic plates. *Journal of Applied Mechanics*, 12(2):A69–A77, 1945.
[65] R. Rosencranz and S. Bogen. Clinical laboratory measurement of serum, plasma, and blood viscosity. *American journal of clinical pathology*, 125 Suppl:S78–86, 2006.
[66] S. Roy, L. Heltai, and F. Costanzo. Benchmarking the immersed finite element method for fluid-structure interaction problems. *Computers & Mathematics with Applications*, 69(10):1167–1188, 2015.

[67] T. Sawada and A. Tezuka. LLM and X-FEM based interface modeling of fluid-thin structure interactions on a non-interface-fitted mesh. *Computational Mechanics*, 48(3):319–332, 2011.
[68] J. H. Seo and R. Mittal. A sharp-interface immersed boundary method with improved mass conservation and reduced spurious pressure oscillations. *Journal of Computational Physics*, 230(19):7347–7363, 2011.
[69] A. F. Shinn, M. A. Goodwin, and S.P. Vanka. Immersed boundary computations of shear- and buoyancy-driven flows in complex enclosures. *International Journal of Heat and Mass Transfer*, 52(17):4082–4089, 2009.
[70] P. Singh, D.D. Joseph, T.I. Hesla, R. Glowinski, and T.-W. Pan. A distributed Lagrange multiplier/fictitious domain method for viscoelastic particulate flows. *Journal of Non-Newtonian Fluid Mechanics*, 91(2):165–188, 2000.
[71] K. Stein, T. Tezduyar, and R. Benney. Mesh moving techniques for fluid-structure interactions with large displacements. *Journal of Applied Mechanics*, 70(1):58–63, 2003.
[72] W. Strychalski and R. D. Guy. Intracellular pressure dynamics in blebbing cells. *Biophysical Journal*, 110(5):1168–1179, 2016.
[73] K. Takizawa and T. E. Tezduyar. Computational methods for parachute fluid–structure interactions. *Archives of Computational Methods in Engineering*, 19(1):125–169, 2012.
[74] K. Takizawa, Y. Bazilevs, and T. E. Tezduyar. Space–time and ale-vms techniques for patient-specific cardiovascular fluid–structure interaction modeling. *Archives of Computational Methods in Engineering*, 19(2):171–225, 2012.
[75] K. Takizawa, T.E. Tezduyar, A. Buscher, and S. Asada. Space-time interface-tracking with topology change (ST-TC). *Computational Mechanics*, 54(4):955–971, 2014.
[76] T. Tezduyar. Stabilized finite element formulations for incompressible flow computations. *Advances in Applied Mechanics*, 28:1–44, 1992.
[77] H. S. Udaykumar, R. Mittal, P. Rampunggoon, and A. Khanna. A sharp interface cartesian grid method for simulating flows with complex moving boundaries. *Journal of Computational Physics*, 174(1):345–380, 2001.
[78] R. Van Loon, P. D. Anderson, F. P. T. Baaijens, and F. N. Van de Vosse. A three-dimensional fluid–structure interaction method for heart valve modelling. *Comptes Rendus Mécanique*, 333(12):856–866, 2005.
[79] X. Wang and L. T. Zhang. Modified immersed finite element method for fully-coupled fluid–structure interactions. *Computer Methods in Applied Mechanics and Engineering*, 267:150–169, 2013.
[80] X. Wang and L.T. Zhang. Interpolation functions in the immersed boundary and finite element methods. *Computational Mechanics*, 45(4): 321–334, 2010.
[81] G. D. Weymouth, D. G. Dommermuth, K. Hendrickson, and D.K.P. Yue. Advancements in Cartesian-grid methods for computational ship hydrodynamics. In *26th Symposium on Naval Hydrodynamics (16/09/06-21/09/06)*, Rome, Italy, 2006.
[82] Th. Wick. Flapping and contact FSI computations with the fluid–solid interface-tracking/interface-capturing technique and mesh adaptivity. *Computational Mechanics*, 53(1):29–43, 2014.
[83] C. Yan, W.X. Huang, G.X. Cui, C. Xu, and Z.S. Zhang. A ghost-cell immersed boundary method for large eddy simulation of flows in complex geometries. *International Journal of Computational Fluid Dynamics*, 29(1):12–25, 2015.
[84] T. Ye, R. Mittal, H. S. Udaykumar, and W. Shyy. An accurate cartesian grid method for viscous incompressible flows with complex immersed boundaries. *Journal of Computational Physics*, 156(2):209–240, 1999.
[85] L. Zhang, A. Gerstenberger, X. Wang, and W. Liu. Immersed finite element method. *Computer Methods in Applied Mechanics and Engineering*, 193:2051–2067, 2004.
[86] A. Zilian and A. Legay. The enriched space-time finite element method (EST) for simultaneous solution of fluid-structure interaction. *International Journal for Numerical Methods in Engineering*, 75(3):305–334, 2008.
[87] S. Zonca, C. Vergara, and L. Formaggia. An unfitted formulation for the interaction of an incompressible fluid with a thick structure via an XFEM/DG approach. *SIAM Journal on Scientific Computing*, 40(1):B59–B84, 2018.